Front. Mech. Eng. 2023, 18(2): 24
https://doi.org/10.1007/s11465-022-0740-0

RESEARCH ARTICLE

Design of a novel side-mounted leg mechanism with high flexibility for a multi-mission quadruped earth rover BJTUBOT

Yifan WU, Sheng GUO (✉), Luquan LI, Lianzheng NIU, Xiao LI

School of Mechanical, Electronic and Control Engineering, Beijing Jiaotong University, Beijing 100044, China

✉ *Corresponding author. E-mail: shguo@bjtu.edu.cn (Sheng GUO)*

ABSTRACT Earth rover is a class of emerging wheeled-leg robots for nature exploration. At present, few methods for these robots' leg design utilize a side-mounted spatial parallel mechanism. Thus, this paper presents a complete design process of a novel 5-degree-of-freedom (5-DOF) hybrid leg mechanism for our quadruped earth rover BJTUBOT. First, a general approach is proposed for constructing the novel leg mechanism. Subsequently, by evaluating the basic locomotion task (LT) of the rover based on screw theory, we determine the desired motion characteristic of the side-mounted leg and carry out its two feasible configurations. With regard to the synthesis method of the parallel mechanism, a family of concise hybrid leg mechanisms using the 6-DOF limbs and an L_{1F1C} limb (which can provide a constraint force and a couple) is designed. In verifying the motion characteristics of this kind of leg, we select a typical (3-U$\underline{P}$RU&$\underline{R}$RRR)&$\underline{R}$ mechanism and then analyze its kinematic model, singularities, velocity mapping, workspace, dexterity, statics, and kinetostatic performance. Furthermore, the virtual quadruped rover equipped with this innovative leg mechanism is built. Various basic and specific LTs of the rover are demonstrated by simulation, which indicates that the flexibility of the legs can help the rover achieve multitasking.

KEYWORDS design synthesis, parallel mechanism, hybrid leg mechanism, screw theory, quadruped robot

1 Introduction

The rapid development of mobile robots has provided a great impetus for natural discovery. In the field of planetary exploration, unmanned rovers [1] have received considerable attention as a potential means to uncover planets far from the earth. In recent decades, numerous Lunar and Mars rovers have been used, which has aroused people's curiosity about these engineering achievements. By contrast, the concept of the Earth rover is unusual and fresh. In distinguishing it from other mobile robots, we can classify the Earth rover as an automatic all-terrain vehicle designed centered on the earth exploration missions. Based on this definition, some test prototypes of Mars rovers can be provisionally identified as Earth rovers. In achieving all-terrain function, these robots generally use a passive suspension system to connect the wheels to the fuselage: the Mars rover Spirit, Opportunity, and Perseverance [2,3] of the United States, and the Lunar rover Yutu [4] of China all apply the rocker bogie passive suspension structure. Hence, China's Zhurong rover [5] adopts an active suspension concept to swiftly extricate the rover trapped in the sand, whereas the EU ExoMars Rover [6] is also equipped with a collapsible active suspension to gain more flexibility. However, these improved designs focus on achieving reliable missions on exoplanets, and they are far less flexible for executing tasks in the earth environment.

The leg structure can greatly improve the mobility of mobile robots, which has been verified in applications of bionic exploration robots. Hence, the use of a novel leg mechanism to replace the traditional suspension system can be in demand for the earth rover. At present, most legged robots use series structures on their legs. For example, ANYmal [7] uses a 3-degree-of-freedom (3-DOF) leg to walk freely in a narrow mine or in an alpine environment [8,9]. Accordingly, its control algorithm is complex. Bartsch et al. [10] developed a hexapod robot for Lunar exploration. This robot can provide mobility to climb up the crater rim and descend the crater wall.

Received May 8, 2022; accepted September 7, 2022

Similarly, MANTIS [11] also has a multi-mode structure, which results in its manipulation capabilities in unstructured terrain. However, it has 61 actuators, which are difficult to do remote maintenance. In achieving an efficient locomotion on a flat ground, the concept of adding wheels for the legged robot is proposed [12]. Geilinger et al. [13,14] designed legged robot Skaterbots using a wheel on the end of its leg, which can complete smooth skating. ANYmal also tried to add a wheel to the leg structure [15,16], such a design can bring it a speed of 4 m/s and reduce the cost of transport by 83%. Although this combination of a leg and a wheel can be an inspiration for the design of earth rovers, the leg using series structures has no stability advantage in harsh environments.

In enhancing the stability of motion, parallel mechanisms have been applied in the design of a legged robot. Pan and Gao [17] exhibit a six-parallel-legged robot for drilling holes on large parts. Chen et al. [18] designed a fault-tolerant quadruped robot employing a scissors mechanism. The robot of Giewont and Sahin [19] adopts a Delta mechanism for each leg. BITNAZA [20,21] is a wheeled-leg robot with four or six wheels. All of its legs are Stewart mechanism and are arranged perpendicular to the fuselage. Lin and Guo [22,23] designed a legged mobile lander, which can adjust the attitude based on the terrain. In addition to the single use of a parallel structure, the use of hybrid mechanisms can increase the stability and flexibility in robot design [24–26]. PAW [27] is an early form hybrid wheeled-leg robot, which can control the legs to reposition the wheels, but its structure is simple. He and Gao [28] introduced a class of quadruped robots using parallel mechanisms and a passive joint attached to the leg-end. Based on GF set theory, Zhang et al. [29] designed a 3-mixed-DOF protectable leg mechanism for a firefighting multi-legged robot. Cordes et al. [30,31] proposed a hybrid wheeled-leg planetary rover, each of its legs adopts a closed chain connecting a rod structure, which has excellent bearing characteristics, but its motion velocity remains slow. Notably, these aforementioned parallel mechanisms are mounted upside-down on the robot. This design can improve stability, but at the expense of flexibility and workspace.

BJTUBOT is a new type of earth rover that has been investigated in our laboratory for multitasking needs. Considering the performance limitations of existing leg structural forms, this paper provides insights into designing a novel side-mounted hybrid leg mechanism. The innovation point is that this leg design implements an appropriate side-mounted parallel structure as the main part to improve stability. In addition, an extra-integrated revolute (R) joint on the leg can significantly expand the flexible working space, whereas a wheel at the end of the leg can facilitate the quadruped robot to move more rapidly on a flat ground.

2 Approach to constructing the novel leg mechanism

This paper aims to design suitable side-mounted novel leg mechanisms for the quadrupedal earth rover BJTUBOT. The new leg structure should have high spatial motion flexibility to help the rover achieve a multitasking performance. As shown in Fig. 1, the novel leg mechanism is constructed as follows:

Step 1. Determine the motion requirements of the output link of the leg.

Based on the exploration task, the locomotion forms for the rover can be given first. By mounting on the side of the rover, the motion of the output link of the leg should help the fuselage complete these locomotion forms.

Step 2. Design various feasible leg structures under motion requirements.

In general, when the required motion DOF of the leg structure is established, a number of feasible configurations will be identified. Based on the characteristics of the limb structure and drive arrangement, this research aims to provide some general and simple methods to design the leg mechanism under the corresponding boundary conditions.

Step 3. Select and verify a typical new leg mechanism.

Among numerous design forms, a typical new leg structure is selected. Its inverse kinematics, singularity, workspace, dexterity, and mechanics performance should be investigated. In verifying its motion feasibility, the legs are assembled on a virtual prototype of the rover for locomotion simulation. The analysis results can serve as a basis for further optimization.

3 Motion requirements of the leg mechanism design

3.1 Kinematic constraint system of leg mechanism's output link

Normally, the leg output link should have translational and rotational DOFs to make the rover move in three-dimensional space. In depicting the spatial motion of the leg output link, this paper uses screw theory [32–35]. A screw $\$$ consists of two parts, which can represent the direction and position of a vector, such as velocity, angular velocity, force, and torque applied to a rigid body. Therefore, when analyzing complex spatial mechanisms, it can be concise and unified by using screw theory.

As shown in Fig. 2, based on the position characteristics of side mounting, a coordinate system is established on the rover body to study the motion of the leg output link relative to its base (the **right-hand rule** is used in

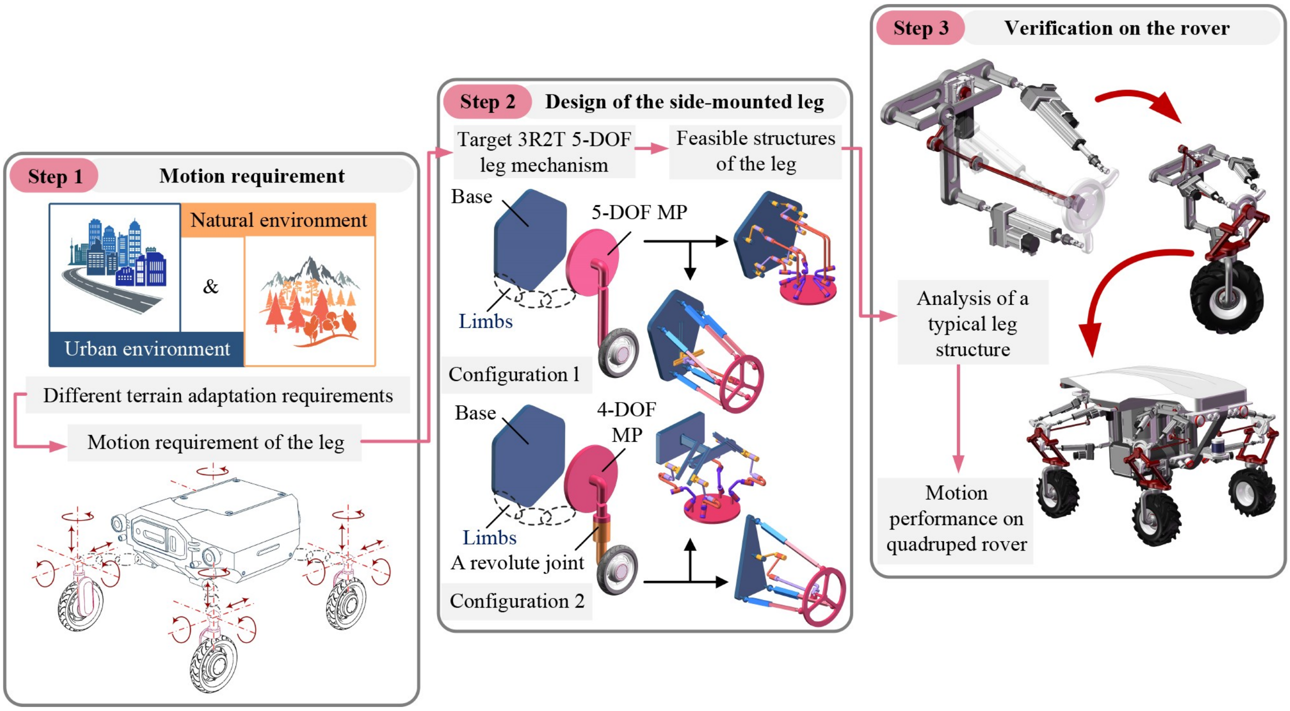

Fig. 1 Concept of constructing a side-mounted novel leg mechanism for our earth rover. DOF: degree-of-freedom, MP: moving platform.

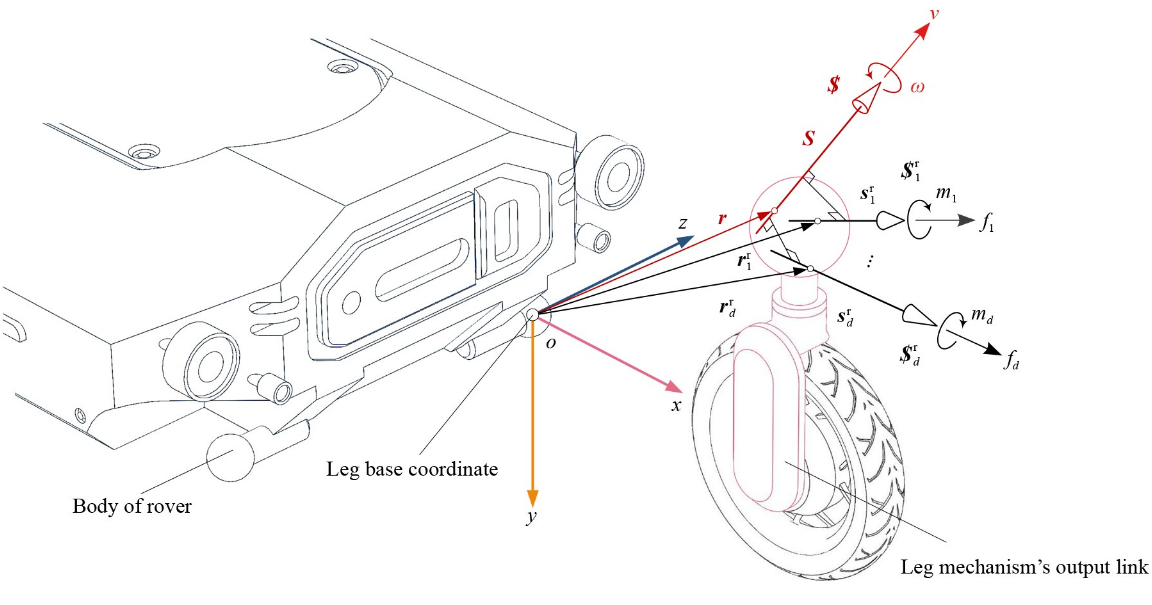

Fig. 2 d-dimensional wrench system on the output link of the side-mounted leg mechanism.

this paper). A d-dimensional wrench system $\boldsymbol{\$}^{\mathrm{r}}$ exerts on the leg output link with the infinitesimal twist $\boldsymbol{\$}$, where d stands for the number of independent constraints in the system. $\boldsymbol{s}$ and $\boldsymbol{r}$ are the corresponding direction and location vectors of the twist $\boldsymbol{\$}$. $\boldsymbol{s}_d^{\mathrm{r}}$ and $\boldsymbol{r}_d^{\mathrm{r}}$ represent the corresponding direction and location vectors of the dth constraint screw $\boldsymbol{\$}_d^{\mathrm{r}}$. Notably, the constraints include the constraint force f and constraint couple m, which are usually provided by other links of the leg mechanism and by the ground (consider that the force or couple provided by the leg can overcome the ground friction). The leg output link can move in unconstrained space, and its motion can be represented by the twist $\boldsymbol{\$}$. Based on screw theory, the wrench system is reciprocal to the twist. Therefore, the platform motion characteristics can be completely determined by the nature of the wrench system, which is the main theoretical basis for designing the mechanical structure of the leg.

3.2 Desired motion of the output link of the leg mechanism

The basic exploration task of the earth rover BJTUBOT can move flexibly on different terrains. In addition, the tasks can be divided into two categories: One is the detection operation in human activity areas, such as rescue assistants, production detection, and security patrols. The other category is the exploration of the natural environment, such as geological exploration or ecological monitoring. The notable features of the implementation environment require the rover to adopt suitable locomotion forms, thereby achieving an efficient multi-tasking. Given the various social and productive activities, extensive cultural features are observed, including gardens, roads, and public buildings. In general, such features all have large flat areas. By contrast, natural terrains can be mostly divided into plains and mountains with rivers, lakes, deserts, and coastal areas. These landscapes alternately form an uneven surface, making it challenging for the rover to perform tasks. The leg design could help the rover move effectively on artificial and natural terrain. Based on this criterion, several basic locomotion tasks (LTs) of our rover are analyzed.

First, in ensuring stability at high speed on flat roads or expressways, the rover has a deployable function to efficiently widen its wheelbase (support polygon). Similar to Fig. 3(a), the initial position of the leg output link in the leg base coordinates can be represented by a vector $\boldsymbol{r} = [rx,\ ry,\ rz]^{\mathrm{T}}$, where rx, ry, and rz are the lengths of $\boldsymbol{r}$ projected onto the x-, y-, and z-axis, respectively. If the leg output link rotates with the twist $\$_1$, where $\boldsymbol{s}_1 = [0,0,1]^{\mathrm{T}}$, then the rover can change the wheelbase with the original direction:

$$\$_1 = \begin{bmatrix} \boldsymbol{s}_1 \\ \boldsymbol{r}\times\boldsymbol{s}_1 \end{bmatrix} = [\ 0,\quad 0,\quad 1,\quad ry,\quad -rx,\quad 0\ ]^{\mathrm{T}}. \tag{1}$$

In narrow roads, factories, parking lots, or valleys, omnidirectional motion is extremely efficient for the rover. As shown in Fig. 3(b), if the leg output link rotates with the twist $\$_2$, where $\boldsymbol{s}_2 = [0,1,0]^{\mathrm{T}}$, then the rover can achieve the omnidirectional motion by changing the direction of each wheel.

$$\$_2 = \begin{bmatrix} \boldsymbol{s}_2 \\ \boldsymbol{r}\times\boldsymbol{s}_2 \end{bmatrix} = [\ 0,\quad 1,\quad 0,\quad -rz,\quad 0,\quad rx\ ]^{\mathrm{T}}. \tag{2}$$

In altering the wheelbase when the rover is moving laterally, the leg output link can rotate in accordance with the twist $\$_3$, where $\boldsymbol{s}_3 = [1,0,0]^{\mathrm{T}}$:

$$\$_3 = \begin{bmatrix} \boldsymbol{s}_3 \\ \boldsymbol{r}\times\boldsymbol{s}_3 \end{bmatrix} = [\ 1,\quad 0,\quad 0,\quad 0,\quad rz,\quad -ry\ ]^{\mathrm{T}}. \tag{3}$$

The steering function is used frequently for the rover. In accomplishing an Ackerman steering, the front two wheels should rotate at a certain angle based on the twist $\$_2$. In achieving pivot steering, all wheels must rotate on the basis of $\$_2$, as shown in Figs. 3(c) and 3(d).

The performance of the suspension system will directly affect vehicle’s handling stability and ride comfort. At present, MacPherson and double wishbone independent suspensions are commonly used in cars [36–38]. As shown in Fig. 4(a), when the rover confronts the fluctuation of terrain, the active suspension can be achieved by making the leg output link move along $\$_4$ and simulate the spring damping system, where $\boldsymbol{s}_4 = [0,1,0]^{\mathrm{T}}$.

$$\$_4 = \begin{bmatrix} \boldsymbol{0} \\ \boldsymbol{s}_4 \end{bmatrix} = [\ 0,\quad 0,\quad 0,\quad 0,\quad 1,\quad 0\ ]^{\mathrm{T}}. \tag{4}$$

When the rover encounters obstacles and cannot drive normally, the walking ability is necessary. As shown in Fig. 4(b), if the leg output link makes translational motion in accordance with $\$_4$ and $\$_5$, where $\boldsymbol{s}_5 = [1,0,0]^{\mathrm{T}}$, then the rover can give a step walking:

$$\$_5 = \begin{bmatrix} \boldsymbol{0} \\ \boldsymbol{s}_5 \end{bmatrix} = [\ 0,\quad 0,\quad 0,\quad 1,\quad 0,\quad 0\ ]^{\mathrm{T}}. \tag{5}$$

Given these five basic motion forms (MFs), combining the used twist, the rover can achieve some more complex motions. As shown in Fig. 5(a), when the rover is trying to pass through the uneven terrain, based on the translation along twists $\$_4$ and $\$_5$, the rotation around twists $\$_1$ and $\$_3$ can substantially expand the workspace and adjust the orientation of the foothold adaptively. As illustrated in Fig. 5(b), after executing the translation along $\$_4$, the implementation of twist $\$_1$ can lower the chassis and then allow the rover to crawl through low obstacles. Similarly, as shown in Fig. 5(c), by allowing motions to cooperate with one another depending on twists $\$_1$, $\$_4$, and $\$_5$, the rover can accomplish a jumping action. In actual operation, different combinations of twists applied to the leg can make the rover obtain varied motion states, which improves the flexibility and multi-selectivity of the motion strategy. Then, the twist system of the leg output link includes $\$_1$, $\$_2$, $\$_3$, $\$_4$, and $\$_5$. A general twist can be given by a linear combination of the five abovementioned basis twists:

$$\$ = k_1\$_1 + k_2\$_2 + k_3\$_3 + k_4\$_4 + k_5\$_5 = [k_1,\quad k_2,\quad k_3,\quad k_5 + k_1 ry - k_2 rz,\quad k_4 - k_1 rx + k_3 rz,\quad k_2 rx - k_3 ry]^{\mathrm{T}}, \tag{6}$$

where k_1, k_2, k_3, k_4, and k_5 can be arbitrary real numbers. Therefore, the wrench of the leg output link is as follows:

$$\$^{\mathrm{r}} = [0,\quad 0,\quad 1,\quad ry,\quad -rx,\quad 0]^{\mathrm{T}}. \tag{7}$$

When $ry = rx = 0$, $\$^{\mathrm{r}} = [0,\ 0,\ 1,\ 0,\ 0,\ 0]^{\mathrm{T}}$.

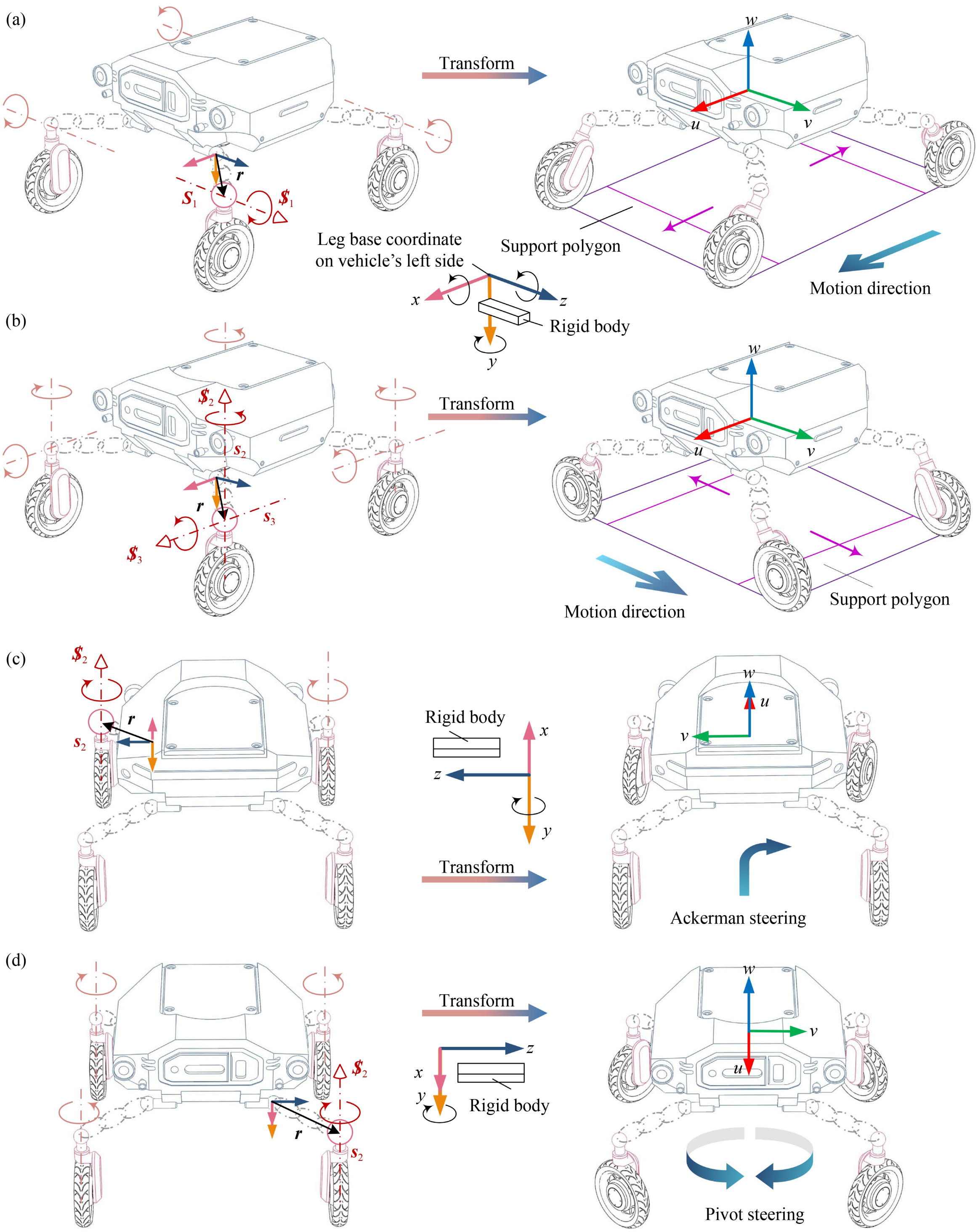

Fig. 3 Motion forms only use rotation degree of freedoms: (a) deployable function, (b) omnidirectional motion, (c) Ackerman steering, and (d) pivot steering.

Consequently, this leg output link should achieve three rotations and two translations, that is, a 3R2T (3 revolute joints and 2 translations) 5-DOF motion. Notably, the use rate and motion range of each twist are different. However, depending on special tasks, the assembly size of parts, and interference conditions, 5-DOF is currently an ideal solution.

4 Design of the novel 3R2T 5-DOF side-mounted leg mechanism

4.1 Two feasible configurations of the desired leg mechanism

As described in Section 3, the motion DOF of the output

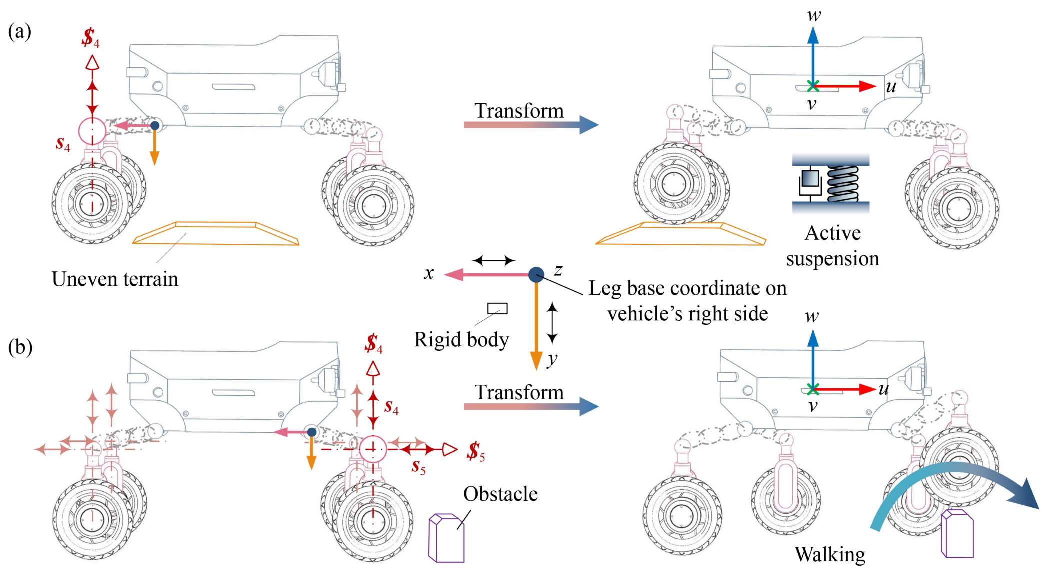

Fig. 4 Motion forms only use translation degree of freedoms: (a) active suspension function and (b) walking motion.

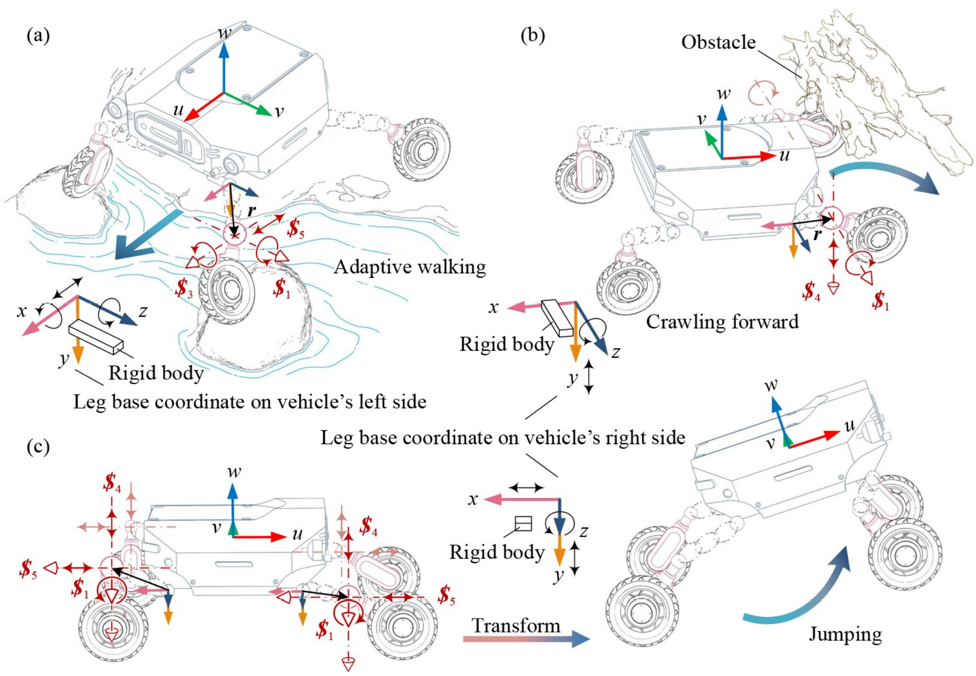

Fig. 5 Special functions combine different motion forms: (a) adaptive walking, (b) crawling, and (c) jumping.

link of the leg mechanism should be 3R2T, that is, the leg output link should be able to rotate around the x-, y-, and z-axis and to translate along the x- and y-axis. In implementing this 5-DOF leg mechanism based on the parallel mechanism, a pure parallel mechanism or a serial-parallel multistage hybrid mechanism can be selected. The series structural transmission chain with two or more joints may lead to more inertial forces, more cumulative errors, and multiple solutions of inverse kinematics. Thus, the following two side-mounted designs of the 5-DOF leg mechanism are prioritized.

(1) If the leg output link is regarded as a moving platform, then this leg can be achieved by a 3R2T side-mounted parallel mechanism. As shown in Fig. 6(a), the wrench of its moving platform is presented as follows:

$$\boldsymbol{\$}^{\mathrm{r}} = [0,\quad 0,\quad 1,\quad 0,\quad 0,\quad 0]^{\mathrm{T}}. \tag{8}$$

(2) As described in Section 3, the usage frequency of the rotational motion by twist $\boldsymbol{\$}_2$ is high, and its range of motion is large. Therefore, a driving joint must be used to provide this rotation, thereby increasing the control efficiency. Hence, this leg can be achieved by a hybrid mechanism with a 2R2T side-mounted parallel mechanism and an R joint serving as a steering device (Fig. 6(b)).

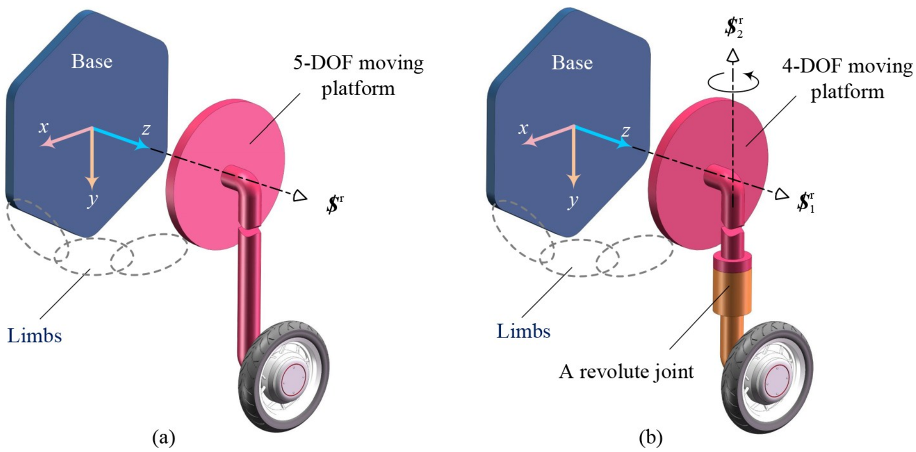

Fig. 6 Wrench of the two feasible configurations of the side-mounted leg mechanism: (a) 5-DOF side-mounted parallel leg mechanism and (b) hybrid leg mechanism using a 4-DOF side-mounted parallel mechanism and a revolute steering joint. DOF: degree-of-freedom.

The wrench of the moving platform is as follows:

$$\begin{cases} \$_1^r = [0, \quad 0, \quad 1, \quad 0, \quad 0, \quad 0]^T, \\ \$_2^r = [0, \quad 0, \quad 0, \quad 0, \quad 1, \quad 0]^T. \end{cases} \tag{9}$$

4.2 Design attempt of the leg using symmetrical structures

In general, the use of a symmetrical structure should be initially considered for the leg because of its good isotropy (Fig. 6(a)). Based on screw theory, Fang and Tsai [39] proposed a synthesis method of 5-DOF symmetrical parallel robot, whereas Li and Huang [40] presented a synthesis method of 4-DOF symmetrical parallel manipulators. The proposed synthesis theories have been authoritative, which can be used to achieve the 3R2T 5-DOF symmetrical parallel mechanism. Using the relevant theory, this paper applies the combination of several F-limbs (the limb provides only one constraint force) [39] with the same structure to construct the mechanism. The R and prismatic (P) joints are the basic joint types used for each limb, and the R joints have two types. Type-1 revolute joints, denoted as R_1, intersect the wrench axis at a common point. Type-2 revolute joints, denoted as R_2, are parallel to the wrench axis. The intersection point of R_1 determines the location of the constraint force, whereas the direction of the constraint force is determined by R_2. Thus, the structure of all F-limbs must satisfy the following conditions to provide only one linearly independent wrench for the moving platform:

C1. All type-1 R joint axes in the F-limbs intersect at a common point.

C2. All type-2 R joint axes in the F-limbs must be parallel to one another, and their direction is consistent with the constraint force $\$^r = [0, \ 0, \ 1, \ 0, \ 0, \ 0]^T$.

Side-mounting the base and arranging the F-limbs based on **C1** and **C2**, some 5-DOF symmetrical parallel mechanisms can be obtained (Fig. 7). In general, these mechanisms have only one driver on each limb, which are complex and have no engineering advantages for a rover.

Next, for the second configuration described in Subsection 4.1 (Fig. 6(b)), the mechanism should be composed of a 2R2T 4-DOF symmetrical parallel mechanism and an R joint in series. Similarly, the following conditions are given to accomplish the parallel mechanism part:

C3. The constraint force contributed by the F-limbs must be parallel and in the same direction.

C4. The constraint force contributed by the F-limbs cannot be collinear.

Based on the abovementioned conditions, some feasible configurations are listed in Fig. 8. When four limbs are used to form the mechanism, the two limbs on one side form a group, and the axes of R_1 joints of each group intersect at one point. However, these leg mechanisms are complex, and their instantaneous motion characteristics may pose challenges for practical applications. Thus, the 4- or 5-DOF symmetrical parallel mechanism is not suitable for the side-mounted leg design of the earth over.

4.3 Design of the novel leg mechanism using asymmetrical structures

In designing a 3R2T 5-DOF asymmetric structure for the leg, the passive constraining limb [41,42] can be used to construct the mechanism. In general, the structural feature of using the passive constraining limb is that one passive limb completely constrains the motion of the platform, whereas several 6-DOF limbs (such as SPS (spherical−prismatic−spherical) and UCU (universal−cylindrical−universal) limbs) provide the driving force. Following this method, the 3R2T 5-DOF asymmetric parallel mechanism can be designed (Fig. 9). Each of the five 6-DOF limbs has an actuator that provides the driving force: One F-limb provides a constraint force along $\$^r = [0, \ 0, \ 1, \ 0, \ 0, \ 0]^T$, and the six limbs can reach the required motion characteristic for the platform.

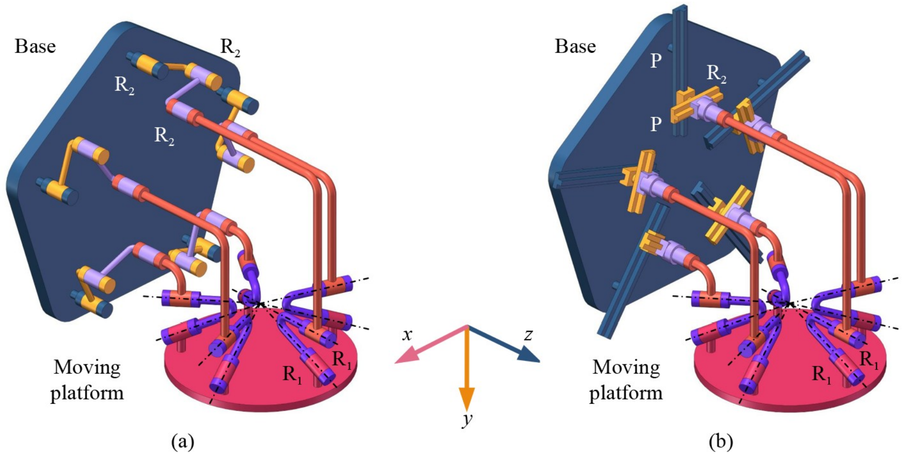

Fig. 7 Some configurations of 3R2T 5-degree-of-freedom parallel mechanisms using a symmetrical structure with F-limbs: (a) 5-5R($R_2R_2R_2R_1R_1$) and (b) 5-3R2P($PPR_2R_1R_1$). P: prismatic joint, R: revolute joint, R_1: type-1 revolute joint, R_2: type-2 revolute joint.

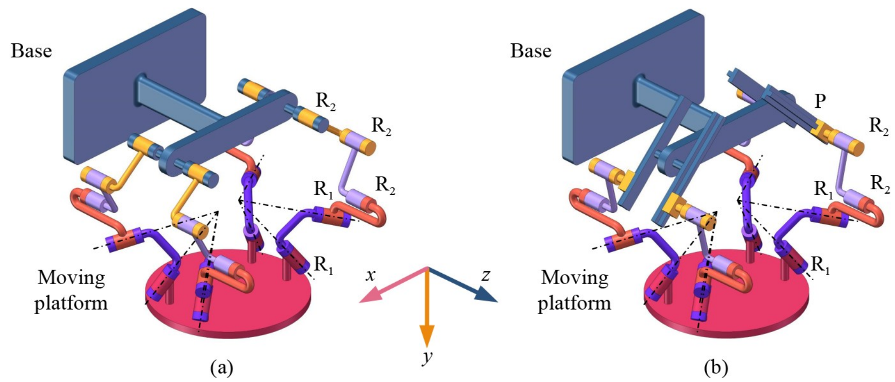

Fig. 8 Some configurations of 2R2T 4-degree-of-freedom parallel mechanisms using a symmetrical structure with F-limbs: (a) 4-5R($R_2R_2R_2R_1R_1$) and (b) 4-4R1P($PR_2R_2R_1R_1$). P: prismatic joint, R: revolute joint, R_1: type-1 revolute joint, R_2: type-2 revolute joint.

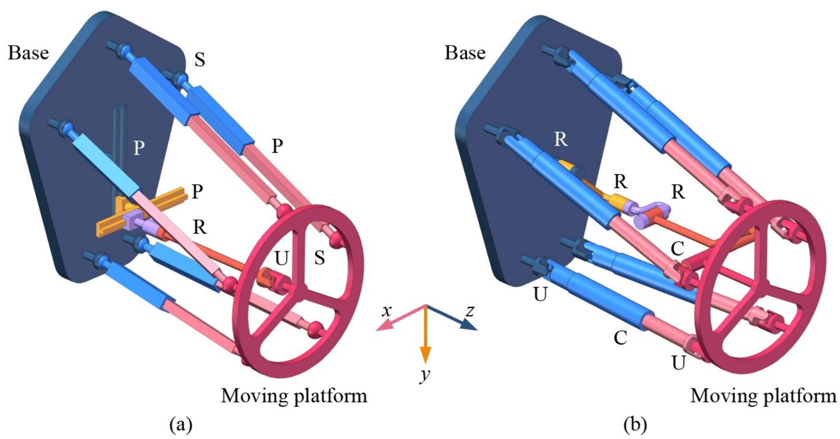

Fig. 9 Two examples of 3R2T 5-DOF asymmetrical parallel mechanisms using passive constraining limb: (a) 5-SPS&PPRU and (b) 5-UCU&RRRC. C: cylindrical joint, P: prismatic joint, R: revolute joint, S: spherical joint, U: universal joint.

When designing the 2R2T 4-DOF asymmetric parallel mechanism, the structure is similar to that of 5-DOF mechanism, but the passive constraining limb should provide the constraint force $\boldsymbol{\$}_1^{\mathrm{r}} = [0,\ 0,\ 1,\ 0,\ 0,\ 0]^{\mathrm{T}}$ and the constraint couple $\boldsymbol{\$}_2^{\mathrm{r}} = [0,\ 0,\ 0,\ 0,\ 1,\ 0]^{\mathrm{T}}$ (as shown in the upper part of Fig. 10). In this paper, this limb is known as an $\mathrm{L_{1F1C}}$ limb. This limb only consists of four basic passive joints, including m R joints and n P joints ($m+n=4$, $n\leqslant 2$). Other types of joints, such as universal joints (U) and cylindrical pairs (C), can be

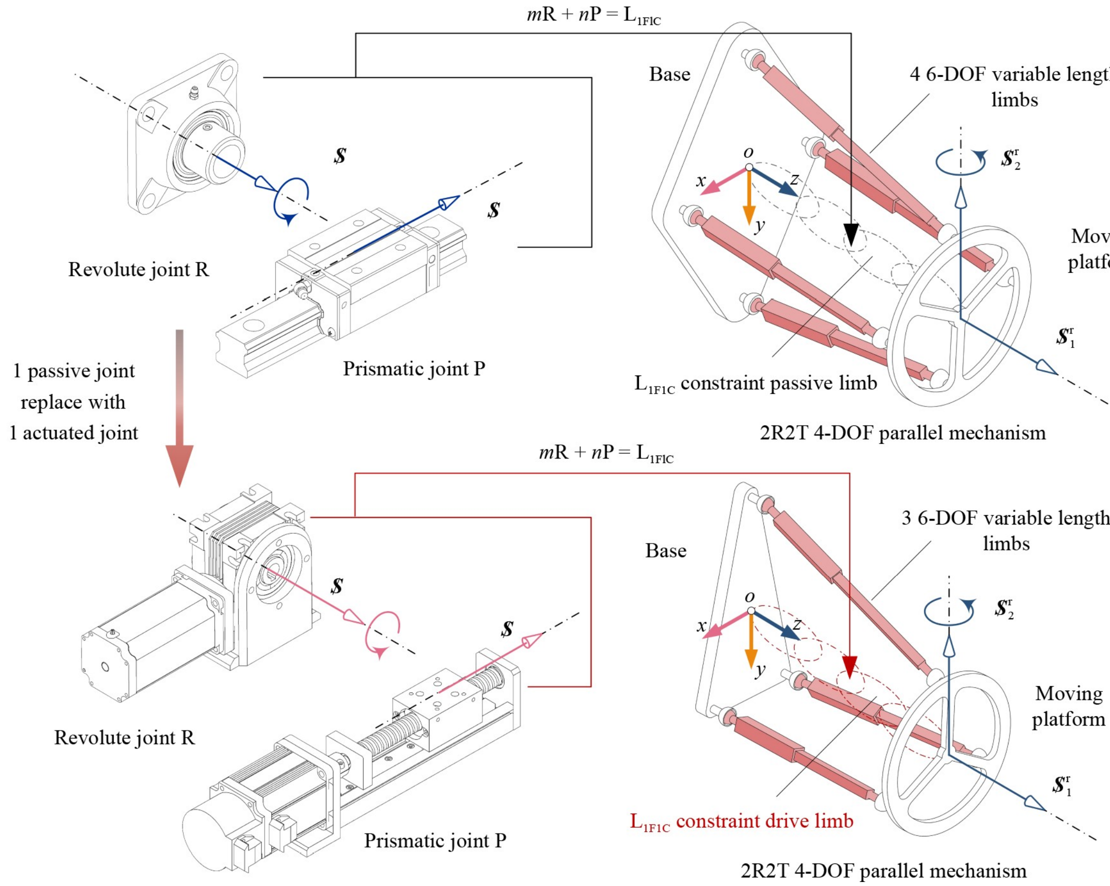

Fig. 10 Construction of the L_{1F1C}-limb. L_{1F1C}: passive constraining limb provides both a constraint force and a constraint couple. DOF: degree-of-freedom.

formed by these two basic joints. The structure of the L_{1F1C} limb must meet the following two conditions:

C5. The axes of its R joints must intersect or be parallel to the constraint force, and they must be perpendicular to the constraint couple.

C6. The axes of its P joints are perpendicular to the constraint force and linearly independent.

Considering the position characteristics of side-mounting, all feasible L_{1F1C} limbs are enumerated in Table 1 for the convenience of design.

Furthermore, when side-mounting, the overall weight of the leg must be considered. Hence, the mechanism will be more concise for engineering applications. Through observation, the number of limbs is greater than the DOF of the platform because the actuator is only assembled on the 6-DOF limbs. Therefore, an actuator can be added in the L_{1F1C} limb to reduce a 6-DOF limb, whereas this L_{1F1C} limb can provide the constraints and partial drives required by the mechanism (as shown in the lower part of Fig. 10). Thus, as shown in Fig. 11, the two 2R2T 4-DOF asymmetric parallel mechanisms all have three 6-DOF variable length limbs and one L_{1F1C} limb. Compared with the mechanism described in Subsection 4.2, this structure family is more concise. In addition, by arranging the limbs, the workspace of the leg can show the characteristics of mirror symmetry. This side-mounted structure is an ideal option that can simultaneously provide flexibility and stability for the legs, which is suitable for the lightweight design of the earth rover.

4.4 Initial boundary conditions of the side-mounted leg mechanism design

By referring to the motion requirements mentioned in Subsection 3.2, we selected an appropriate structure for the novel side-mounted leg mechanism in accordance with the following boundary conditions:

(1) For the moving platform, the angular motion range around $\boldsymbol{\$}_3$ (attitude angle about the x-axis) should be $\alpha \in [-10°, 20°]$; the angular motion range around $\boldsymbol{\$}_2$ (attitude angle about the y-axis) should be $\beta \in [-90°, 90°]$, and the angular motion range around $\boldsymbol{\$}_1$ (attitude angle about the z-axis) should be $\gamma \in [-30°, 30°]$.

(2) When the height of the side-mounted base along the y-axis is h and the width of the side-mounted base along the x-axis is w, the movable distance of the moving platform along the x-axis should be at least $3w/2$, and the movable distance along the y-axis should be $4h/5$. Therefore, motion flexibility must be ensured, and space occupancy must be reduced.

Table 1 Feasible L_{1F1C} limbs for side-mounting

Joint type	4R feasible limbs	3R1P feasible limbs	2R2P feasible limbs
Only exists basic joints	$R_1R_1R_1R_2$, $R_1R_1R_2R_2$, $R_1R_2R_2R_2$	$R_1R_1R_2P$, $R_1R_1PR_2$, $R_1R_2R_2P$, $R_1R_2PR_2$, $R_1PR_2R_2$, $R_2R_2R_1P$	R_1R_2PP, R_1PR_2P, R_1PPR_2
Exists equivalent cylindrical pairs	–	R_1CR_2, CR_2R_2	CRP, CRP
Exists equivalent universal joints	R_1R_1U, R_1UR_2, UR_2R_2	RUP, URP, UPR	UPP

Note: Joints arranged in reverse order, known as the kinematic inversion, are not included.

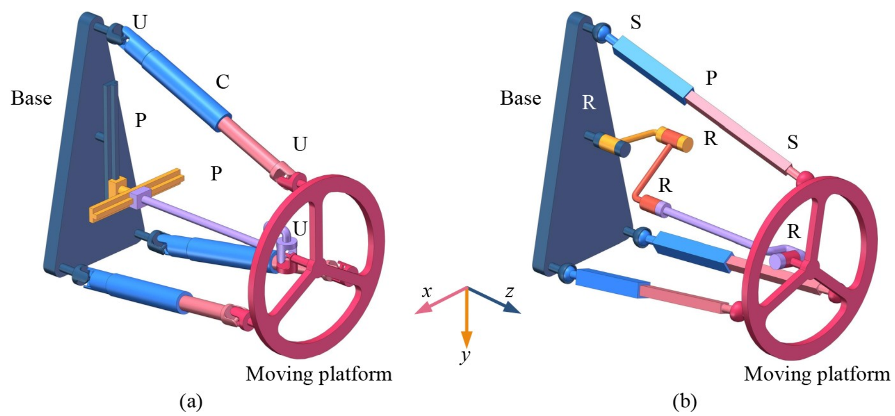

Fig. 11 Two examples of 2R2T 4-degree-of-freedom asymmetrical parallel mechanisms using the L_{1F1C} limb: (a) 3-UCU&PPU and (b) 3-SPS&RRRR. C: cylindrical joint, P: prismatic joint, R: revolute joint, S: spherical joint, U: universal joint.

(3) In ensuring a simple structure, low cost, easy maintenance, and appropriate stiffness, fewer limbs and joints must be used. Given the stress characteristics of side-mounting, U pair must be used instead of S joint in 6-DOF limbs.

(4) In ensuring that the control scheme is simple and reliable, one drive must be adopted on each limb, and less P joints must be used in the L_{1F1C} limb.

Based on the abovementioned conditions, we preselected a (3-U$\underline{\text{P}}$RU&$\underline{\text{R}}$RRR)&$\underline{\text{R}}$ hybrid leg mechanism as the research object, where $\underline{\text{P}}$ means the prismatic joint with actuation and $\underline{\text{R}}$ stands for the revolute joint with actuation. This typical mechanism conforms to the second configuration described in Subsection 4.1. It consists of a 3-U$\underline{\text{P}}$RU&$\underline{\text{R}}$RRR 4-DOF side-mounted parallel mechanism that belongs to the mechanism family (Fig. 11) and a steering R joint connecting with the wheel. The conceptual diagram of the mechanism is shown in Fig. 12.

5 Performance analysis of the novel side-mounted 3R2T 5-DOF leg mechanism

5.1 Kinematic analysis

Kinematics is an indispensable part of mechanism design. Position analysis can reflect the control difficulty of the mechanism, whereas singularity analysis can provide reference for the arrangement of the limbs.

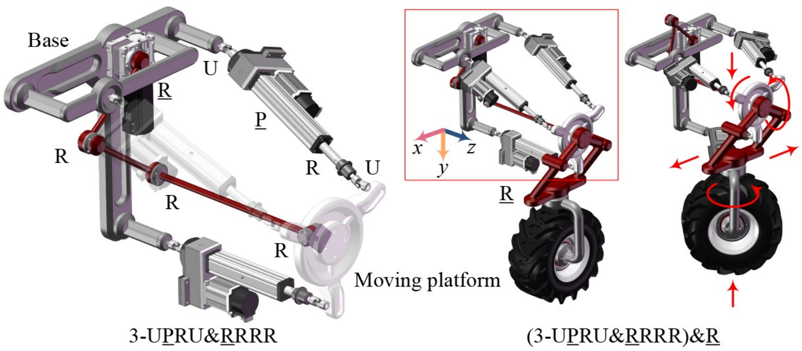

Fig. 12 Conceptual diagram of the side-mounted (3-U<u>P</u>RU&<u>R</u>RRR)&<u>R</u> hybrid leg mechanism. P: prismatic joint, <u>P</u>: prismatic joint with actuation, R: revolute joint, <u>R</u>: revolute joint with actuation, U: universal joint.

5.1.1 Position analysis of the 3-U<u>P</u>RU&<u>R</u>RRR side-mounted parallel mechanism

The 3-U<u>P</u>RU&<u>R</u>RRR mechanism is the core part of the leg, and its inverse kinematics is described as follows. As shown in Fig. 13, the base coordinate system x–y–z is located at the original point O_B, and its x-axis connects the starting point of the two U<u>P</u>RU limbs, whereas its z-axis is perpendicular to the base plane. The moving platform coordinate system x_P–y_P–z_P is located at the center point O_P of the moving platform. Its x_P-axis always coincides with the axis of the last joint in the <u>R</u>RRR limb, whereas its z_P-axis is perpendicular to the moving platform. The moving platform can only rotate around its x_P- and z_P-axis under the structural constraints, and the rotation angles are α' $(-\pi/2 < \alpha' < \pi/2)$ and γ' $(-\pi/2 < \gamma' < \pi/2)$. We use ${}^{B}\boldsymbol{v}$ to represent a vector $\boldsymbol{v}$ in the base coordinate, ${}^{P}\boldsymbol{v}$ to represent a vector in the moving platform coordinate and ${}^{W}\boldsymbol{v}$ to represent a vector in the wheel coordinate. The position of the platform in the base frame is defined as ${}^{B}\boldsymbol{p} = [p_x, p_y, p_z]^{T}$. α, β, and γ are the attitude angles of the platform relative to the x-, y-, and z-axis of the base frame. The length l_i (i = 1, 2, 3) of the drive <u>P</u> joint (there we define it the length of the vector $\left|\overrightarrow{A_iB_i}\right|$) in the U<u>P</u>RU limbs and the rotation angle θ of the <u>R</u> joint in the <u>R</u>RRR limb must be functions of the variables α, β, γ, and ${}^{B}\boldsymbol{p}$. For example, the rotation matrix ${}^{B}\boldsymbol{R}_{P}$ is used to define the orientation of the moving platform in the base coordinate system. For the U<u>P</u>RU limb, we define $\boldsymbol{a}_i = \overrightarrow{O_BA_i}$, $\boldsymbol{b}_i = \overrightarrow{O_PB_i}$, $\boldsymbol{p} = \overrightarrow{O_BO_P}$, $l_i = \left|\overrightarrow{A_iB_i}\right|$ and assume that $\boldsymbol{u}_{li}$ is the unit vector of <u>P</u> joint. Then, the closed-loop equation is defined as follows:

$$ {}^{B}\boldsymbol{p} = {}^{B}\boldsymbol{a}_i + \left|\overrightarrow{A_iB_i}\right| {}^{B}\boldsymbol{u}_{li} - {}^{B}\boldsymbol{b}_i = {}^{B}\boldsymbol{a}_i + l_i {}^{B}\boldsymbol{u}_{li} - {}^{B}\boldsymbol{R}_{P} {}^{P}\boldsymbol{b}_i, \tag{10} $$

$$ l_i {}^{B}\boldsymbol{u}_{li} = {}^{B}\boldsymbol{p} - {}^{B}\boldsymbol{a}_i + {}^{B}\boldsymbol{R}_{P} {}^{P}\boldsymbol{b}_i. \tag{11} $$

In eliminating ${}^{B}\boldsymbol{u}_{li}$, both sides of the abovementioned equation can be multiplied by themselves:

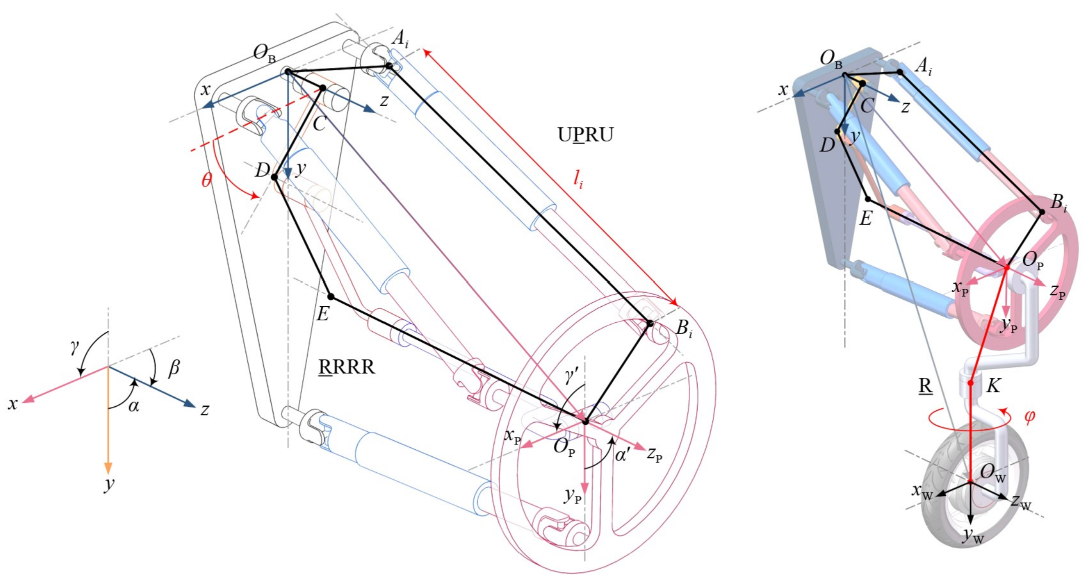

Fig. 13 Schema diagram of the 3-U<u>P</u>RU&<u>R</u>RRR parallel mechanism (left) and the (3-U<u>P</u>RU&<u>R</u>RRR)&<u>R</u> hybrid leg mechanism (right). <u>P</u>: prismatic joint with actuation, R: revolute joint, <u>R</u>: revolute joint with actuation, U: universal joint.

$$l_i^2 = \left|{}^{\mathrm{B}}\boldsymbol{p} - {}^{\mathrm{B}}\boldsymbol{a}_i + {}^{\mathrm{B}}\boldsymbol{R}_{\mathrm{P}}{}^{\mathrm{P}}\boldsymbol{b}_i\right|^2. \tag{12}$$

Then,

$$l_i = \left|{}^{\mathrm{B}}\boldsymbol{p} - {}^{\mathrm{B}}\boldsymbol{a}_i + {}^{\mathrm{B}}\boldsymbol{R}_{\mathrm{P}}{}^{\mathrm{P}}\boldsymbol{b}_i\right|,\ \ l_i > 0. \tag{13}$$

For the R̲RRR limb, its first three joints are parallel to one another, whereas the fourth joint is perpendicular to other joints. We define $\boldsymbol{d} = \overrightarrow{CD}$, $\boldsymbol{e} = \overrightarrow{DE}$ and assume that $\boldsymbol{u}_d = [\cos\theta, \sin\theta, 0]^{\mathrm{T}}$ is the unit vector of the linkage CD (CD is connected with R̲ joint). Given the geometric constraints, θ $(-\pi/2 < \theta < \pi)$ can be solved using a simpler geometric method. Using the cosine theorem, we obtain the following equations:

$$|\boldsymbol{e}|^2 = |\boldsymbol{d}|^2 + p_x^2 + p_y^2 - 2|\boldsymbol{d}|\cdot\sqrt{p_x^2+p_y^2}\cos\angle DCE, \tag{14}$$

$$\angle DCE = \arccos\frac{p_x^2+p_y^2+|\boldsymbol{d}|^2-|\boldsymbol{e}|^2}{2|\boldsymbol{d}|\sqrt{p_x^2+p_y^2}},\ \angle DCE \in (0,\ \pi). \tag{15}$$

Then, θ can be calculated as follows:

$$\theta = \arctan\frac{p_y}{p_x} - \angle DCE,\ \arctan\frac{p_y}{p_x} \in (0,\ \pi). \tag{16}$$

5.1.2 Position analysis of the (3-UP̲RU&R̲RRR)&R̲ hybrid leg mechanism

Next, we analyze the inverse kinematics of the hybrid leg mechanism (3-UP̲RU&R̲RRR)&R̲. Given the orientation and position of the leg-end (i.e., the center of the wheel), l_i $(i = 1, 2, 3)$, θ, and the rotation angle φ of the steering R̲ joint connected with the leg-end must be obtained. The position vector of the leg-end in the base coordinate is ${}^{\mathrm{B}}\boldsymbol{p}_{\mathrm{W}}$. As shown in Fig. 13, we define the center of the steering R̲ joint as K and the center of the leg-end (i.e., wheel) as O_{W}. We define $\boldsymbol{k} = \overrightarrow{O_{\mathrm{P}}K}$, $\boldsymbol{w} = \overrightarrow{KO_{\mathrm{W}}}$, and $\boldsymbol{p}_{\mathrm{W}} = \overrightarrow{O_{\mathrm{B}}O_{\mathrm{W}}}$. The rotation matrix ${}^{\mathrm{P}}\boldsymbol{R}_{\mathrm{W}}$ is used to solve the orientation of the leg-end in the moving platform frame, whereas the rotation matrix ${}^{\mathrm{B}}\boldsymbol{R}_{\mathrm{W}}$ is used to define the orientation of the leg-end in the base frame. Notably, ${}^{\mathrm{P}}\boldsymbol{R}_{\mathrm{W}}=\mathrm{Rot}(y,\ \varphi)$ (rotate φ about the y-axis), and ${}^{\mathrm{B}}\boldsymbol{R}_{\mathrm{W}}$ can be obtained as follows:

$$\begin{aligned}{}^{\mathrm{B}}\boldsymbol{R}_{\mathrm{W}} &= \mathrm{Rot}(x_{\mathrm{P}},\ \alpha')\cdot\mathrm{Rot}(y,\ \varphi)\cdot\mathrm{Rot}(z_{\mathrm{P}},\ \gamma') \\ &= \begin{bmatrix} \mathrm{c}\varphi\mathrm{c}\gamma' & -\mathrm{c}\varphi\mathrm{s}\gamma' & \mathrm{s}\varphi \\ \mathrm{c}\alpha'\mathrm{s}\gamma' + \mathrm{s}\alpha'\mathrm{c}\gamma'\mathrm{s}\varphi & \mathrm{c}\alpha'\mathrm{c}\gamma' - \mathrm{s}\alpha'\mathrm{s}\varphi\mathrm{s}\gamma' & -\mathrm{s}\alpha'\mathrm{c}\varphi \\ \mathrm{s}\alpha'\mathrm{s}\gamma' - \mathrm{c}\alpha'\mathrm{c}\gamma'\mathrm{s}\varphi & \mathrm{s}\alpha'\mathrm{c}\gamma' + \mathrm{c}\alpha'\mathrm{s}\varphi\mathrm{s}\gamma' & \mathrm{c}\alpha'\mathrm{c}\varphi \end{bmatrix},\end{aligned} \tag{17}$$

where c stands for cos and s for sin. If $\mathrm{c}\alpha' > 0$ at $[-\pi/2,\ \pi/2]$, then we can calculate φ by $\mathrm{s}\varphi$ and $\mathrm{c}\alpha'\mathrm{c}\varphi$ in ${}^{\mathrm{B}}\boldsymbol{R}_{\mathrm{W}}$.

The closed-loop equation is defined as follows:

$$\begin{aligned}{}^{\mathrm{B}}\boldsymbol{p}_{\mathrm{W}} &= {}^{\mathrm{B}}\boldsymbol{p} + {}^{\mathrm{B}}\boldsymbol{k} + {}^{\mathrm{B}}\boldsymbol{w} = {}^{\mathrm{B}}\boldsymbol{p} + {}^{\mathrm{B}}\boldsymbol{R}_{\mathrm{W}}({}^{\mathrm{W}}\boldsymbol{k} + {}^{\mathrm{W}}\boldsymbol{w}) \\ &= {}^{\mathrm{B}}\boldsymbol{p} + {}^{\mathrm{B}}\boldsymbol{R}_{\mathrm{W}}({}^{\mathrm{W}}\boldsymbol{R}_{\mathrm{P}}{}^{\mathrm{P}}\boldsymbol{k} + {}^{\mathrm{W}}\boldsymbol{w}),\end{aligned} \tag{18}$$

$${}^{\mathrm{B}}\boldsymbol{p} = {}^{\mathrm{B}}\boldsymbol{p}_{\mathrm{W}} - {}^{\mathrm{B}}\boldsymbol{R}_{\mathrm{W}}({}^{\mathrm{W}}\boldsymbol{R}_{\mathrm{P}}{}^{\mathrm{P}}\boldsymbol{k} + {}^{\mathrm{W}}\boldsymbol{w}), \tag{19}$$

where ${}^{\mathrm{W}}\boldsymbol{R}_{\mathrm{P}}$ is the inverse of ${}^{\mathrm{P}}\boldsymbol{R}_{\mathrm{W}}$.

Then, for limb UP̲RU, the following equation is obtained:

$$\boldsymbol{p}_{\mathrm{W}} = {}^{\mathrm{B}}\boldsymbol{a}_i + l_i{}^{\mathrm{B}}\boldsymbol{u}_{li} + {}^{\mathrm{B}}\boldsymbol{R}_{\mathrm{P}}{}^{\mathrm{P}}\boldsymbol{b}_i + {}^{\mathrm{B}}\boldsymbol{R}_{\mathrm{W}}({}^{\mathrm{W}}\boldsymbol{R}_{\mathrm{P}}{}^{\mathrm{P}}\boldsymbol{k} + {}^{\mathrm{W}}\boldsymbol{w}). \tag{20}$$

Similar to Eq. (13), there is

$$l_i = \left|{}^{\mathrm{B}}\boldsymbol{a}_i - \boldsymbol{p}_{\mathrm{W}} + {}^{\mathrm{B}}\boldsymbol{R}_{\mathrm{P}}{}^{\mathrm{P}}\boldsymbol{b}_i + {}^{\mathrm{B}}\boldsymbol{R}_{\mathrm{W}}({}^{\mathrm{W}}\boldsymbol{R}_{\mathrm{P}}{}^{\mathrm{P}}\boldsymbol{k} + {}^{\mathrm{W}}\boldsymbol{w})\right|. \tag{21}$$

Hence, for limb R̲RRR, after obtaining ${}^{\mathrm{B}}\boldsymbol{p}$ from Eq. (19), θ can be directly solved by using Eqs. (14)–(16).

5.1.3 Singularity analysis of the 3-UP̲RU&R̲RRR mechanism

The 3-UP̲RU&R̲RRR mechanism (Fig. 14) is the main driving part of the leg. It affects the control difficulty of the whole leg, and its potential singularity may cause the leg to abruptly lose or gain DOF during use, thereby affecting the safe locomotion of the rover. Consequently, the Jacobian matrix must be constructed for analysis [42–44].

Each limb in the parallel mechanism can be regarded as an open-loop chain composed of several basic joints that connect the moving platform to the base. Therefore, the instantaneous twist of the moving platform can be written as follows:

$$\boldsymbol{\$}_{\mathrm{p}} = \dot{\boldsymbol{X}} = \begin{bmatrix} {}^{\mathrm{B}}\boldsymbol{\omega} \\ {}^{\mathrm{B}}\boldsymbol{v}_{O_{\mathrm{P}}} \end{bmatrix} = \sum_{j=1}^{n}\dot{q}_{ij}\boldsymbol{\$}_{ij} = [\boldsymbol{\$}_{i1},\ \boldsymbol{\$}_{i2}, ..., \boldsymbol{\$}_{in}]\begin{bmatrix} \dot{q}_{i1} \\ \dot{q}_{i2} \\ \vdots \\ \dot{q}_{in} \end{bmatrix},$$
$$(i = 1, 2, ..., m), \tag{22}$$

where $\dot{\boldsymbol{X}}$ is the velocity of the moving platform, ${}^{\mathrm{B}}\boldsymbol{\omega}$ is the angular velocity, and ${}^{\mathrm{B}}\boldsymbol{v}_{O_{\mathrm{P}}}$ is the linear velocity of the moving platform in the base coordinate system. If the parallel mechanism has m limbs and each limb has n basic joints, then $\dot{q}_{ij}$ $(j = 1, 2, ..., n)$ denotes the intensity and $\boldsymbol{\$}_{ij}$ $(j = 1, 2, ..., n)$ represents the unit screw of the jth joint in the ith limb.

Based on Eq. (19), we initially analyze the UP̲RU 6-DOF limb. As shown in Fig. 14(a), each UP̲RU limb has a linear actuator, and the other joints are all passive, including the R joints composed in the U joints. The instantaneous twist $\boldsymbol{\$}_{\mathrm{P}}$ is defined as the velocity of the moving platform, and then the ith UP̲RU limb is defined as follows:

$$\boldsymbol{\$}_{\mathrm{P}} = \dot{\theta}_{i1}\boldsymbol{\$}_{i1} + \dot{\theta}_{i2}\boldsymbol{\$}_{i2} + \dot{l}_i\boldsymbol{\$}_{i3} + \dot{\theta}_{i4}\boldsymbol{\$}_{i4} + \dot{\theta}_{i5}\boldsymbol{\$}_{i5} + \dot{\theta}_{i6}\boldsymbol{\$}_{i6},\ (i = 1, 2, 3), \tag{23}$$

where $\boldsymbol{\$}_{i1} = \begin{bmatrix} \boldsymbol{s}_{i1} \\ (\boldsymbol{b}_i - \boldsymbol{l}_i)\times\boldsymbol{s}_{i1} \end{bmatrix}$, $\boldsymbol{\$}_{i2} = \begin{bmatrix} \boldsymbol{s}_{i2} \\ (\boldsymbol{b}_i - \boldsymbol{l}_i)\times\boldsymbol{s}_{i2} \end{bmatrix}$, $\boldsymbol{\$}_{i3} = \begin{bmatrix} \boldsymbol{0}_{3\times1} \\ \boldsymbol{s}_{i3} \end{bmatrix}$, $\boldsymbol{\$}_{i4} = \begin{bmatrix} \boldsymbol{s}_{i3} \\ (\boldsymbol{b}_i - \boldsymbol{l}_i)\times\boldsymbol{s}_{i3} \end{bmatrix}$, $\boldsymbol{\$}_{i5} = \begin{bmatrix} \boldsymbol{s}_{i5} \\ \boldsymbol{b}_i\times\boldsymbol{s}_{i5} \end{bmatrix}$, and $\boldsymbol{\$}_{i6} = \begin{bmatrix} \boldsymbol{s}_{i6} \\ \boldsymbol{b}_i\times\boldsymbol{s}_{i6} \end{bmatrix}$.

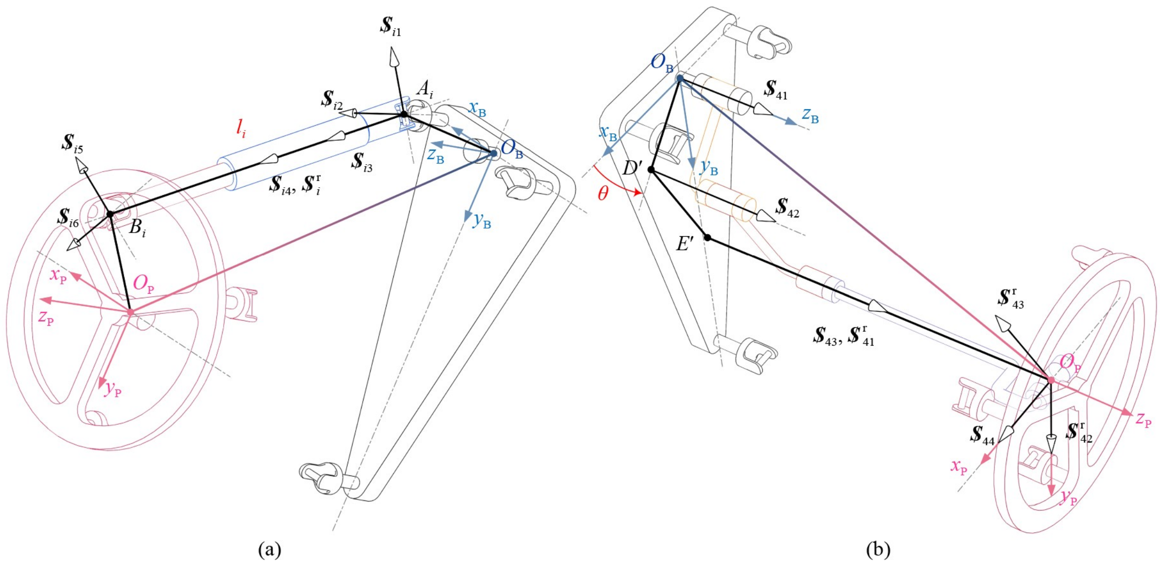

Fig. 14 Schematic diagram of the limbs in the 3-UPRU&RRRR parallel mechanism: (a) UPRU limb and (b) RRRR limb.

$\dot{l}_i$ is the linear velocity of the P joint, $\dot{\theta}_{in}$ $(n = 1,2,...,6)$ is the intensity (there is the angular velocity) of the passive joints, and $\boldsymbol{s}_{ij}$ is the direction vector of $\$_{ij}$, $\boldsymbol{b}_i = \overrightarrow{O_\mathrm{P}B_i}$ and $\boldsymbol{l}_i = \overrightarrow{A_iB_i}$. Correspondingly, these six twists have no screw reciprocal. Next, the P joint in this UPRU limb is locked, and then the reciprocal screws for the limb can form a one-system. The only screw in this system is defined as follows:

$$\$_i^\mathrm{r} = \begin{bmatrix} \boldsymbol{s}_{i3} & \boldsymbol{b}_i \times \boldsymbol{s}_{i3} \end{bmatrix}^\mathrm{T}. \tag{24}$$

Taking the orthogonal product of both sides of Eq. (23) with $\$_i^\mathrm{r}$, we obtain

$$\$_i^{\mathrm{rT}}\left(\Delta \$_\mathrm{p}\right) = \dot{l}_i, \ \ (i = 1,2,3), \tag{25}$$

where $\Delta = \begin{bmatrix} \boldsymbol{0}_{3\times3} & \boldsymbol{E}_{3\times3} \\ \boldsymbol{E}_{3\times3} & \boldsymbol{0}_{3\times3} \end{bmatrix}$ is a symmetric matrix, and $\boldsymbol{E}$ is the dentity matrix.

Then, we can deduce an equation of all UPRU limbs, and get the vector $\dot{\boldsymbol{L}}$ which contains all velocities of the P joints:

$$\boldsymbol{J}_{\mathrm{k\_UPRU}}\$_\mathrm{P} = \begin{bmatrix} (\boldsymbol{b}_1 \times \boldsymbol{s}_{13})^\mathrm{T} & \boldsymbol{s}_{13}^\mathrm{T} \\ (\boldsymbol{b}_2 \times \boldsymbol{s}_{23})^\mathrm{T} & \boldsymbol{s}_{23}^\mathrm{T} \\ (\boldsymbol{b}_3 \times \boldsymbol{s}_{33})^\mathrm{T} & \boldsymbol{s}_{33}^\mathrm{T} \end{bmatrix} \times \$_\mathrm{P} = \begin{bmatrix} \dot{l}_1 \\ \dot{l}_2 \\ \dot{l}_3 \end{bmatrix} = \dot{\boldsymbol{L}}. \tag{26}$$

To date, $\boldsymbol{J}_{\mathrm{k\_UPRU}}$ is the actuation Jacobian for the UPRU limbs. Next, we analyze the RRRR limb. Similar to Eq. (23), we obtain

$$\$_\mathrm{P} = \dot{\theta}\$_{41} + \dot{\theta}_{42}\$_{42} + \dot{\theta}_{43}\$_{43} + \dot{\theta}_{44}\$_{44}, \tag{27}$$

where $\$_{41} = \begin{bmatrix} \boldsymbol{s}_{41} \\ -\boldsymbol{e}' \times \boldsymbol{s}_{41} \end{bmatrix}$, $\$_{42} = \begin{bmatrix} \boldsymbol{s}_{42} \\ \boldsymbol{d}' - \boldsymbol{e}' \times \boldsymbol{s}_{42} \end{bmatrix}$, $\$_{43} = \begin{bmatrix} \boldsymbol{s}_{43} \\ \boldsymbol{0}_{3\times1} \end{bmatrix}$, and $\$_{44} = \begin{bmatrix} \boldsymbol{s}_{44} \\ \boldsymbol{0}_{3\times1} \end{bmatrix}$.

$\dot{\theta}$ is the angular velocity of active R joint; $\dot{\theta}_{42}$, $\dot{\theta}_{43}$, and $\dot{\theta}_{44}$ are the angular velocity of the remaining passive joints. $\boldsymbol{d}' = \overrightarrow{O_\mathrm{B}D'}$ and $\boldsymbol{e}' = \overrightarrow{O_\mathrm{B}E'}$ (D' and E' are the intersection points of $\$_{42}$ and $\$_{43}$ with the base plane, respectively). Notably, there is an infinite pitch screw $\$_{42}^\mathrm{r}$ that is orthogonal to $\$_{41}$, $\$_{42}$, $\$_{43}$, and $\$_{44}$, $\boldsymbol{s}_{42}^\mathrm{r}$ is orthogonal to $\boldsymbol{s}_{44}$ and on the moving platform plane. Then, the reciprocal screws of this four-system are defined as $\$_{41}^\mathrm{r} = \begin{bmatrix} \boldsymbol{s}_{43} \\ \boldsymbol{0}_{3\times1} \end{bmatrix}$ and $\$_{42}^\mathrm{r} = \begin{bmatrix} \boldsymbol{0}_{3\times1} \\ \boldsymbol{s}_{42}^\mathrm{r} \end{bmatrix}$.

Taking the orthogonal product of both sides of Eq. (27) with $\$_{41}^\mathrm{r}$ and $\$_{42}^\mathrm{r}$, we can obtain

$$\$_{4j}^{\mathrm{rT}}(\Delta\$_\mathrm{P}) = 0, \ \ (j = 1,2). \tag{28}$$

The abovementioned equation is written in matrix form:

$$\boldsymbol{J}_{\mathrm{c\_RRRR}}\$_\mathrm{P} = \begin{bmatrix} \boldsymbol{0}_{1\times3} & \boldsymbol{s}_{43}^\mathrm{T} \\ \boldsymbol{s}_{42}^{\mathrm{rT}} & \boldsymbol{0}_{1\times3} \end{bmatrix} \times \$_\mathrm{P} = 0. \tag{29}$$

Then, $\boldsymbol{J}_{\mathrm{c\_RRRR}}$ is the constraint Jacobian for the RRRR limb.

After locking the active joint in the RRRR limb, an additional screw $\$_{43}^\mathrm{r}$ is reciprocal to all the passive joint screws. The $\$_{43}^\mathrm{r}$ is coplanar with $\$_{42}$, $\$_{43}$, and $\$_{44}$ (it can take $\boldsymbol{s}_{43}^\mathrm{r} = \dfrac{\boldsymbol{d}' - \boldsymbol{e}'}{|\boldsymbol{d}' - \boldsymbol{e}'|}$), then

$$\$_{43}^\mathrm{r} = \begin{bmatrix} \boldsymbol{s}_{43}^\mathrm{r} \\ \boldsymbol{0}_{3\times1} \end{bmatrix}. \tag{30}$$

Taking the orthogonal product of both sides of Eq. (27) with $\$_{43}^\mathrm{r}$, the relational equation between the RRRR limb driver velocity and moving platform's twist is defined as follows:

$$\begin{aligned} &\$_{43}^{\mathrm{rT}}(\Delta\$_\mathrm{P}) = (\boldsymbol{s}_{43}^\mathrm{r} \cdot (-\boldsymbol{e}' \times \boldsymbol{s}_{41}))\dot{\theta} \\ &\Rightarrow \$_{43}^{\mathrm{rT}}\Delta\$_\mathrm{P} \big/ (\boldsymbol{s}_{43}^\mathrm{r} \cdot (-\boldsymbol{e}' \times \boldsymbol{s}_{41})) = \dot{\theta}. \end{aligned} \tag{31}$$

Integrating Eqs. (26), (29), and (31), we can obtain the following Jacobian matrix of the 3-UPRU&RRRR parallel mechanism:

$$\boldsymbol{J}\$_{\mathrm{P}}=\begin{bmatrix}(\boldsymbol{b}_1\times\boldsymbol{s}_{13})^{\mathrm{T}} & \boldsymbol{s}_{13}^{\mathrm{T}}\\(\boldsymbol{b}_2\times\boldsymbol{s}_{23})^{\mathrm{T}} & \boldsymbol{s}_{23}^{\mathrm{T}}\\(\boldsymbol{b}_3\times\boldsymbol{s}_{33})^{\mathrm{T}} & \boldsymbol{s}_{33}^{\mathrm{T}}\\\boldsymbol{0}_{1\times3} & (\boldsymbol{s}_{43}^{\mathrm{r}}/(\boldsymbol{s}_{43}^{\mathrm{r}}\cdot(-\boldsymbol{e}'\times\boldsymbol{s}_{41})))^{\mathrm{T}}\\\boldsymbol{0}_{1\times3} & \boldsymbol{s}_{43}^{\mathrm{T}}\\\boldsymbol{s}_{42}^{\mathrm{rT}} & \boldsymbol{0}_{1\times3}\end{bmatrix}\times\$_{\mathrm{P}}=\begin{bmatrix}\dot{l}_1\\\dot{l}_2\\\dot{l}_3\\\dot{\theta}\\0\\0\end{bmatrix}=\dot{\boldsymbol{Q}},\tag{32}$$

where the first four rows of $\boldsymbol{J}$ comprise the actuation Jacobian submatrix, and the last two rows represent the constrained Jacobian submatrix. $\dot{\boldsymbol{Q}}$ is the (6×1) vector, which contains the velocities of all joints.

Based on the Jacobian matrix, some apparent singular configurations can be pointed out. Based on the first three rows of the matrix $\boldsymbol{J}$, if they are linearly correlated, then the manipulator will be under the architecture singularity. Thus, the three UPRU limbs are parallel to one another (Fig. 15(a)). Architecture singularity also occurs when the first three screws and fifth screws become linearly dependent (Figs. 15(b) and 15(c)), where the axial vectors of the four limbs intersect at one point or the actual rank of the four axial vectors is three.

Moreover, the fourth row of the $\boldsymbol{J}$ is observed. If $\boldsymbol{s}_{43}^{\mathrm{r}}\cdot(-\boldsymbol{e}'\times\boldsymbol{s}_{41})=0$, then it will lead to inverse kinematic singularity of the 3-UPRU&RRRR parallel mechanism. Two situations can explain this singularity: (1) If $\boldsymbol{s}_{43}^{\mathrm{r}}=\begin{bmatrix}0&0&0\end{bmatrix}^{\mathrm{T}}$, which indicates that the first joint and the third joint of the RRRR are concentric, then the position of second joint is arbitrary (Fig. 15(d)); (2) if $\boldsymbol{s}_{43}^{\mathrm{r}}\perp(-\boldsymbol{e}'\times\boldsymbol{s}_{41})$, then $\overrightarrow{O_{\mathrm{B}}D'}$ and $\overrightarrow{D'E'}$ are collinear (Fig. 14(b)), and the moving platform cannot move along $\overrightarrow{O_{\mathrm{B}}E'}$. This situation is illustrated in Figs. 15(e) and 15(f). In addition, the mechanism will not have a constraint singularity configuration because the last two rows of $\boldsymbol{J}$ cannot be linearly correlated. The potential occurrence of the abovementioned singular configurations can provide guidance for the reasonable design of the side-mounted leg.

After obtaining the inverse kinematic model and the Jacobian matrix of the 3-UPRU&RRRR side-mounted parallel mechanism, velocity mapping between its moving platform and the actuators can be established. Based on the design requirements of BJTUBOT, the overall size of the 3-UPRU&RRRR mechanism is within the range of 600 mm $\times$ 600 mm $\times$ 600 mm. Thus, the engineering design of each component of the mechanism is carried out, and the corresponding structural parameters of the model are listed in Table 2. Figure 16 shows the velocity mapping analysis of the side-mounted mechanism. The mechanism model is constructed using MATLAB (Fig. 16(a)), and the initial configuration of the moving platform is as follows: $\alpha=\beta=\gamma=0$, $x=-120$ mm, $y=200$ mm, and $z=582$ mm. Under the constraint, the moving platform cannot rotate around its

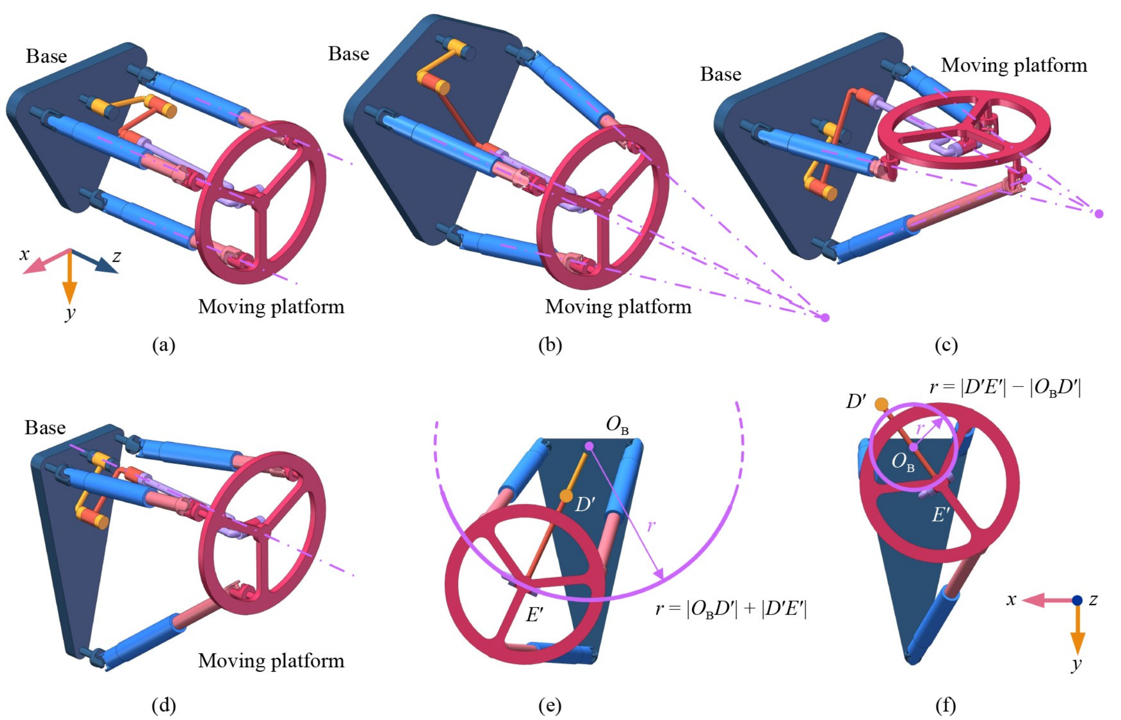

Fig. 15 Singularity configurations of the side-mounted 3-UPRU&RRRR mechanism: (a) three UPRU limbs are parallel, (b) the axial vectors of all limbs intersect at one point, (c) the rank of the of all limbs' axial vectors is less than four, (d) the 1st and 2nd joints of the RRRR limb are concentric, (e) $O_{\mathrm{B}}D'$ and $D'E'$ are stretching collinear, and (f) $O_{\mathrm{B}}D'$ and $D'E'$ are folding collinear.

Table 2 Important structural parameters of the 3-U$\underline{\text{P}}$RU&$\underline{\text{R}}$RRR mechanism

Structural parameter	Value/mm
${}^{\mathrm{B}}\overrightarrow{O_{\mathrm{B}}A_i}$	${}^{\mathrm{B}}\overrightarrow{O_{\mathrm{B}}A_1}=[175,\ 0,\ 170.5]^{\mathrm{T}}$, ${}^{\mathrm{B}}\overrightarrow{O_{\mathrm{B}}A_2}=[-175,\ 0,\ 170.5]^{\mathrm{T}}$, ${}^{\mathrm{B}}\overrightarrow{O_{\mathrm{B}}A_3}=[0,\ 420,\ 170.5]^{\mathrm{T}}$
$\left\lvert\overrightarrow{O_{\mathrm{B}}D'}\right\rvert$	220
$\left\lvert\overrightarrow{D'E'}\right\rvert$	225
$\left\lvert\overrightarrow{E'O_{\mathrm{P}}}\right\rvert$	582
${}^{\mathrm{P}}\overrightarrow{O_{\mathrm{P}}B_i}$	${}^{\mathrm{P}}\overrightarrow{O_{\mathrm{P}}B_1}=[-80\sqrt{3},\ -80,\ 21.5]^{\mathrm{T}}$, ${}^{\mathrm{P}}\overrightarrow{O_{\mathrm{P}}B_2}=[80\sqrt{3},\ -80,\ 21.5]^{\mathrm{T}}$, ${}^{\mathrm{P}}\overrightarrow{O_{\mathrm{P}}B_3}=[0,\ 160,\ 21.5]^{\mathrm{T}}$

own y-axis. Within 300 s, the platform must follow a test trajectory according to the time t. In detail, its position function on the x-axis is $x(t)$, its position function on the y-axis is $y(t)$, its orientation function about α' is $\alpha'(t)$ and its orientation function about γ' is $\gamma'(t)$:

$$\begin{cases} x(t)=t, \\ y(t)=60\sin\left(\dfrac{\pi}{50}t\right)+200, \\ \alpha'(t)=\dfrac{\pi}{6}\sin\left(\dfrac{\pi}{50}t\right), \\ \gamma'(t)=\dfrac{\pi}{6}\sin\left(\dfrac{\pi}{100}t\right). \end{cases} \tag{33}$$

By solving inverse kinematics and differentiating, the position and velocity of each drive joints can be obtained real time (Figs. 16(e) and 16(f)). Using the actual speed of the moving platform (Fig. 16(d)) and the Jacobian matrix, the velocity of each drive joint can also be directly calculated. The validity of the Jacobian matrix can be verified by comparing the error between the calculated and actual velocities of the drive joints. In addition, by observing the velocity mapping between the moving platform and drivers, the speed curves of the drivers are continuous and smooth, and no sudden change is observed. All results can approve the control efficiency of the concise structural design.

5.2 Workspace analysis of the side-mounted leg

In verifying the locomotion capacity of the side-mounted leg mechanism, workspace is an extremely important factor.

First, assuming that the $\underline{\text{P}}$ joint length l_i of each U$\underline{\text{P}}$RU limb meets the limits: $l_{\min} \leqslant l_i \leqslant l_{\max}$ ($i = 1, 2, 3$, $l_{\min}$ = 433 mm, $l_{\max}$ = 533 mm). Then, using the structural parameters shown in Table 2, the workspace of the 3-U$\underline{\text{P}}$RU&$\underline{\text{R}}$RRR mechanism is computed in MATLAB by using the traversal method (Fig. 17(a)). Constrained by the $\underline{\text{R}}$RRR limb, the workspace is located on a plane on the side of the rover. If we set the motion limits to avoid potential interference or singularities, then it will further reduce the effective workspace. Moreover, the reachable workspace of the moving platform depends on its current attitude angle α' and γ' (Figs. 17(b)–17(f)). When controlling the motion of the moving platform, these influencing factors should be considered. This side-located planar workspace can be used directly for efficient gait trajectory planning during walking tasks.

Afterward, we analyze the workspace of the whole (3-U$\underline{\text{P}}$RU&$\underline{\text{R}}$RRR)&$\underline{\text{R}}$ hybrid leg mechanism. As shown in Fig. 13, the position of the leg-end in the moving platform frame can be expressed as ${}^{\mathrm{P}}\overrightarrow{O_{\mathrm{P}}O_{\mathrm{W}}}=[0, 602, -152.5]^{\mathrm{T}}$. Although the workspace of the moving platform is located in a side-located plane, the workspace of the leg-end is a spatial geometry because of the three rotational DOFs (Fig. 18(a)). This finding reflects the contribution of $\$_1$ and $\$_3$ to the leg's flexibility. If motion limitations are not considered, then its workspace can be larger (Fig. 18(b)). The top, left, and front view of the workspace are shown in Figs. 18(c)–18(e). Considering that the center point of the leg-end is designed to be located on the rotation axis of the steering R joint, the leg-end can reach all positions at any angle φ in the workspace. Based on the distribution characteristics of the spatial workspace, the side-mounted legs likely interfere with one another than the inverted legs. This design can effectively improve the flexibility of the leg and reduce the difficulty of the control algorithm.

5.3 Dexterity and global performance analysis

In evaluating the kinematic performance of the side-mounted leg, the dexterity of its 3-U$\underline{\text{P}}$RU&$\underline{\text{R}}$RRR mechanism should be analyzed [45]. Dexterity primarily reflects the possible mapping distortion between the input speed of the drive and the output speed of the moving platform, as well as the motion/force transmission characteristics. Mechanisms with good dexterity tend to have a longer service life. Using Eq. (32), the relative deviation between $\dot{\boldsymbol{Q}}$ and $\boldsymbol{\$}_{\mathrm{P}}$ can be defined as follows:

$$\frac{\|\delta\boldsymbol{\$}_{\mathrm{P}}\|}{\|\boldsymbol{\$}_{\mathrm{P}}\|} \leqslant \|\boldsymbol{J}\|\|\boldsymbol{J}^{-1}\|\frac{\|\delta\dot{\boldsymbol{Q}}\|}{\|\dot{\boldsymbol{Q}}\|}, \tag{34}$$

where $\delta\dot{\boldsymbol{Q}}$ is the driving velocity deviation, $\delta\boldsymbol{\$}_{\mathrm{P}}$ is the velocity deviation of the moving platform, and $\|\boldsymbol{A}\|$ is the Frobenius norm of matrix $\boldsymbol{A}_{m\times n}$. If each element of matrix $\boldsymbol{A}$ is a_{ij}, then

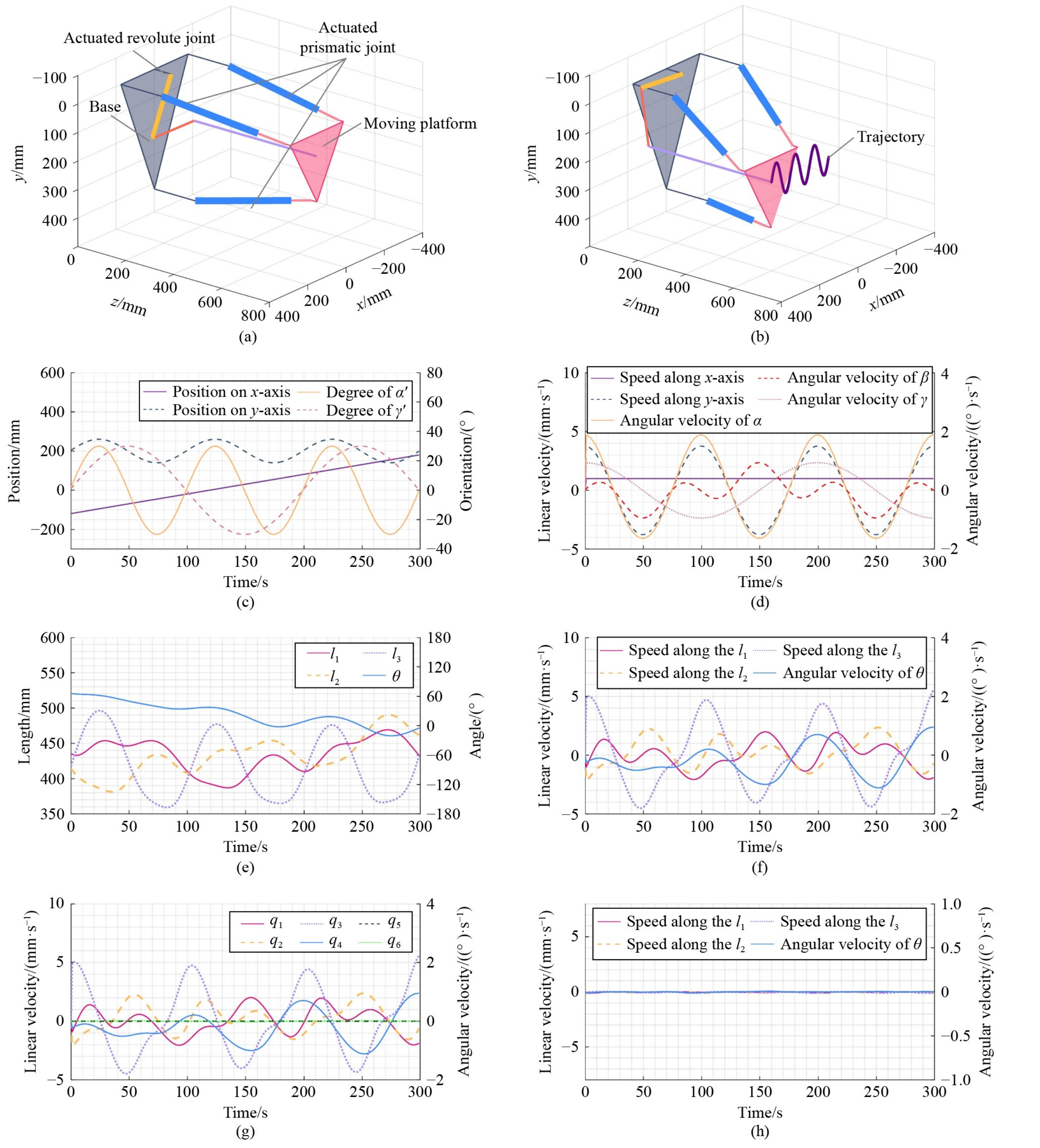

Fig. 16 Velocity mapping analysis of the side-mounted 3-UPRU&RRRR mechanism: (a) initial configuration of the mechanism, (b) desired trajectory of the moving platform, (c) position and orientation curve of the moving platform, (d) velocity curve of the moving platform, (e) driver position curve, (f) driver actual speed curve, (g) driver calculated speed curve, and (h) error between the actual and calculated driver speed. q_i (i = 1,2,…,6) are the six virtual drive joints considered when calculating the driving speed through the Jacobian matrix, in which q_1 corresponds to l_1, q_2 to l_2, q_3 to l_3, and q_4 to θ, while q_5 and q_6 do not correspond to any drive joints in the mechanism, they are only for analysis.

$$\|\boldsymbol{A}\| = \sqrt{\sum_{i=1}^{m}\sum_{j=1}^{n}|a_{ij}|^2}. \tag{35}$$

$k(\boldsymbol{J}) = \|\boldsymbol{J}\|\|\boldsymbol{J}^{-1}\|$ in Eq. (34) is known as the condition number of the Jacobian matrix $\boldsymbol{J}$, and its reciprocal is known as the dexterity or the local condition index (LCI).

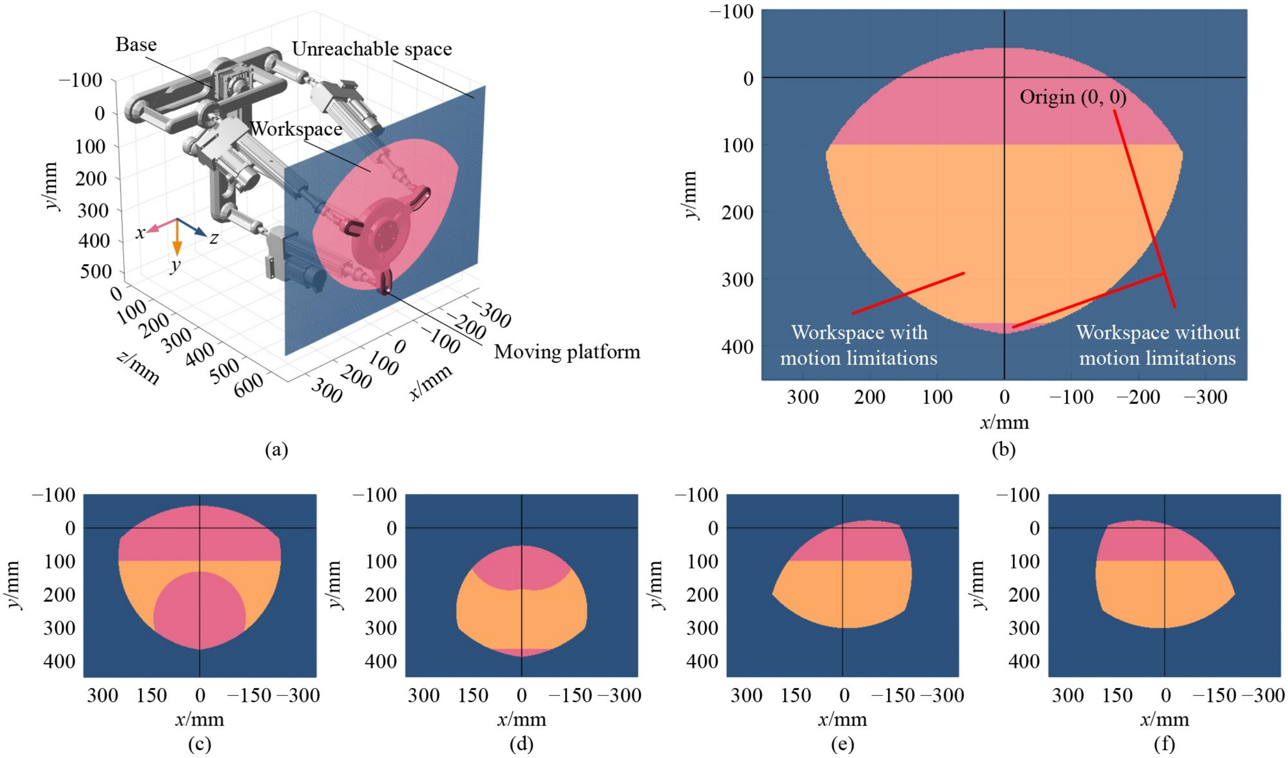

Fig. 17 Workspace of the side-mounted 3-UPRU&RRRR parallel mechanism: (a) $\alpha' = 0$, $\gamma' = 0$ in spatial view, (b) $\alpha' = 0$, $\gamma' = 0$ in plane, (c) $\alpha' = -10°$, $\gamma' = 0$ in plane, (d) $\alpha' = 20°$, $\gamma' = 0$ in plane, (e) $\alpha' = 0$, $\gamma' = -30°$ in plane, and (f) $\alpha' = 0$, $\gamma' = 30°$ in plane.

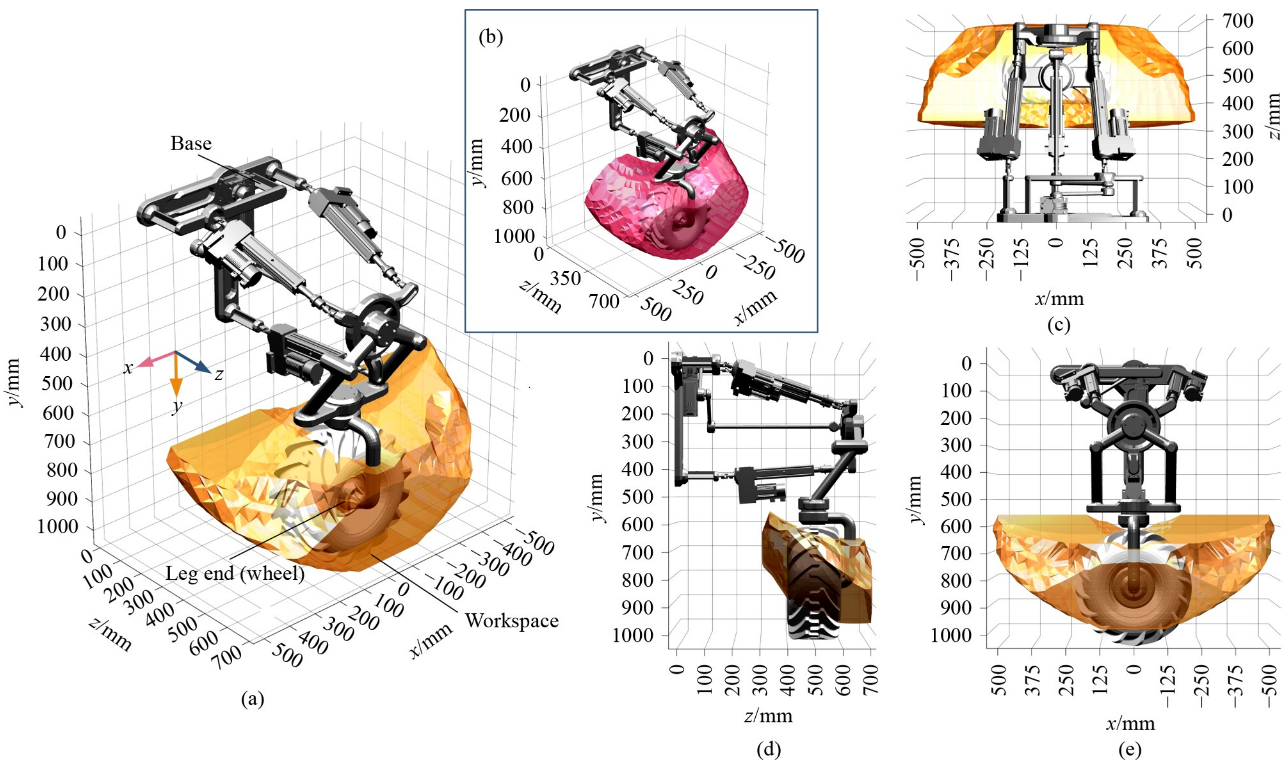

Fig. 18 Workspace of the 3-UPRU&RRRR hybrid leg mechanism: (a) in spatial view, (b) in spatial view without limitations, (c) top view, (d) left view, and (e) front view.

$$\mathrm{LCI} = \frac{1}{k(\boldsymbol{J})}. \tag{36}$$

In general, $0 \leqslant \mathrm{LCI} \leqslant 1$, the larger the LCI, the better the dexterity of the mechanism. When LCI = 0, the mechanism is in a singular configuration. When LCI = 1, the mechanism exhibits the best motion transfer performance, which is known as isotropic. Based on Eq. (36), based on the workspace (mechanical interference restrictions are not considered), the dexterity of the 3-UPRU&RRRR mechanism was calculated in the initial and each ultimate pose (Fig. 19).

As shown in the figure, the dexterity of the mechanism in the working space is greater than zero. As the attitude angle α' of the moving platform increases, the dexterity also increases. Notably, the dexterity of the mechanism can provide a reference for trajectory planning and selecting a transition posture of the moving platform. For example, if the attitude angle γ' of the moving platform is close to the limits of −30° and 30°, then the trajectory should be avoided from the position with poor dexterity to enhance motion accuracy.

Furthermore, in evaluating the overall kinematic performance of the 3-UPRU&RRRR mechanism in a given posture, the global conditioning index (GCI) can be analyzed. GCI was proposed by Gosselin and Angeles [46]. The velocity of the moving platform can be written as follows $\boldsymbol{\$}_{\mathrm{P}} = [{}^{\mathrm{B}}\boldsymbol{\omega}, {}^{\mathrm{B}}\boldsymbol{v}_{O_{\mathrm{P}}}]^{\mathrm{T}}$, and then Eq. (32) can also be written as follows:

$$\dot{\boldsymbol{Q}} = \boldsymbol{J}\boldsymbol{\$}_{\mathrm{P}} = \begin{bmatrix} \boldsymbol{J}_{\omega} & \boldsymbol{J}_{v} \end{bmatrix} \begin{bmatrix} {}^{\mathrm{B}}\boldsymbol{\omega} \\ {}^{\mathrm{B}}\boldsymbol{v}_{O_{\mathrm{P}}} \end{bmatrix} = [\boldsymbol{J}_{\omega}][{}^{\mathrm{B}}\boldsymbol{\omega}] + [\boldsymbol{J}_{v}][{}^{\mathrm{B}}\boldsymbol{v}_{O_{\mathrm{P}}}], \tag{37}$$

where $\boldsymbol{J}_{\omega}$ is the angular velocity mapping part of $\boldsymbol{J}$, and $\boldsymbol{J}_{v}$ is the linear velocity mapping part of $\boldsymbol{J}$.

Their condition number is defined as follows:

$$k(\boldsymbol{J}_{\omega}) = \|\boldsymbol{J}_{\omega}\|\|\boldsymbol{J}_{\omega}^{-1}\|, \tag{38}$$

$$k(\boldsymbol{J}_{v}) = \|\boldsymbol{J}_{v}\|\|\boldsymbol{J}_{v}^{-1}\|. \tag{39}$$

Then, the following GCI of the linear and angular motion of the mechanism η_v and η_ω are proposed as follows:

$$\eta_{\omega} = \frac{\int_{WS} \frac{1}{k(\boldsymbol{J}_{\omega})} \mathrm{d}WS}{\int_{WS} \mathrm{d}WS}, \tag{40}$$

$$\eta_{v} = \frac{\int_{WS} \frac{1}{k(\boldsymbol{J}_{v})} \mathrm{d}WS}{\int_{WS} \mathrm{d}WS}, \tag{41}$$

where WS is the workspace under the current posture condition.

The mathematical meaning of the GCI is the average value of the condition number of the Jacobian matrix over the workspace, $0 \leqslant \eta_i < 1$ $(i = \omega, v)$. Notably, the larger η_i is, the better the motion performance of the mechanism is and the higher the motion accuracy is.

Considering attitude angles α' and γ' as variables, the GCI of the 3-UPRU&RRRR mechanism is demonstrated in Fig. 20. η_ω and η_v indicate that the overall motion performance of the mechanism is good, and the linear motion performance is better than that of the angular motion.

As the main component of the side-mounted leg, the 3-UPRU&RRRR mechanism has good kinematic performance based on the dexterity and GCI analysis.

5.4 Static and kinetostatic simulation analysis

In this research, the leg structure has a side-mounted

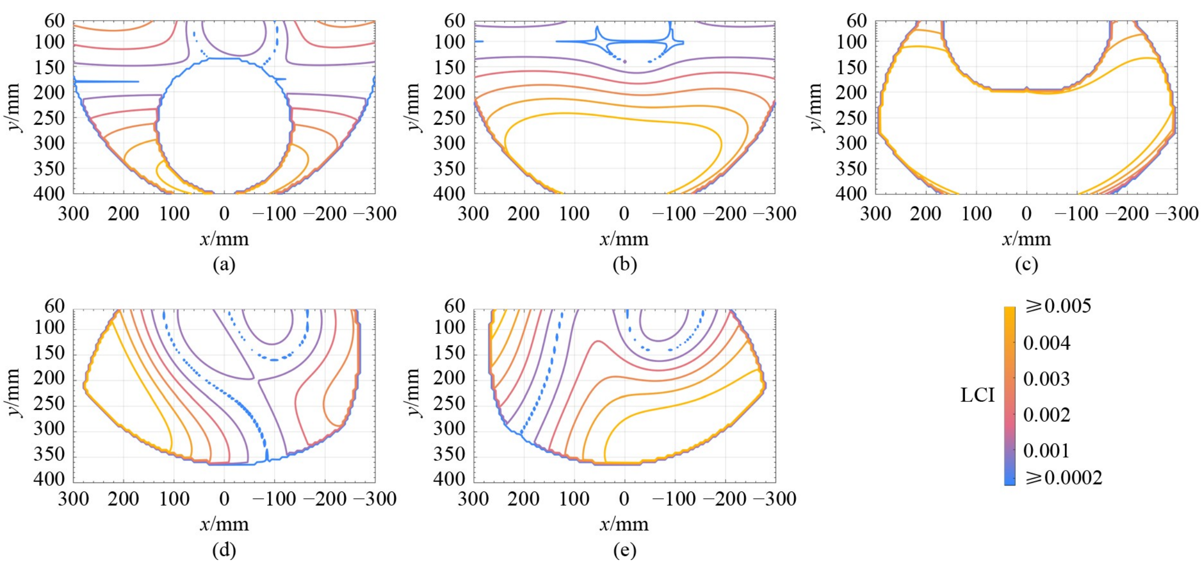

Fig. 19 Dexterity map of the 3-UPRU&RRRR mechanism in initial posture and ultimate posture: (a) $\alpha' = -10°$, $\gamma' = 0°$, (b) $\alpha' = 0°$, $\gamma' = 0°$, (c) $\alpha' = 20°$, $\gamma' = 0°$, (d) $\alpha' = 0°$, $\gamma' = -30°$, and (e) $\alpha' = 0°$, $\gamma' = 30°$. LCI: local condition index.

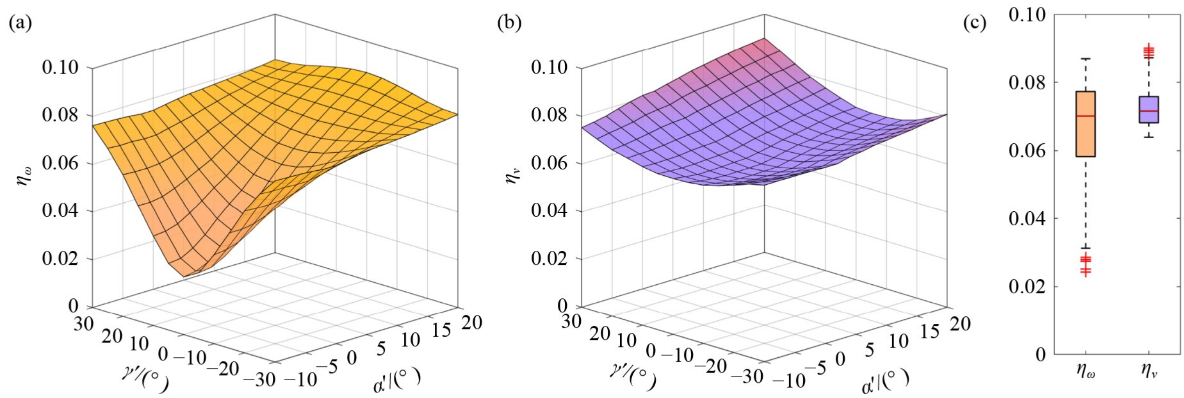

Fig. 20 Global conditioning index of the 3-U<u>P</u>RU&<u>R</u>RRR mechanism under different postures: (a) η_ω, (b) η_v, and (c) boxplot of η_ω and η_v.

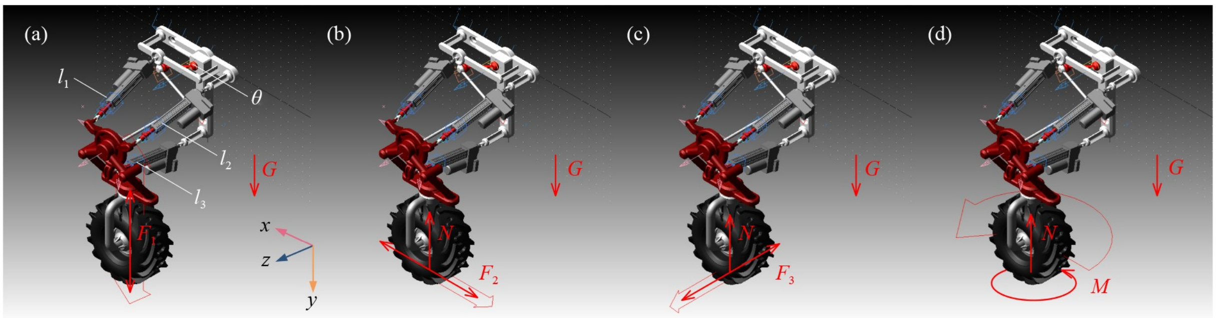

Fig. 21 Static simulation of the side-mounted leg under different common force conditions: (a) condition 1, (b) condition 2, (c) condition 3, and (d) condition 4.

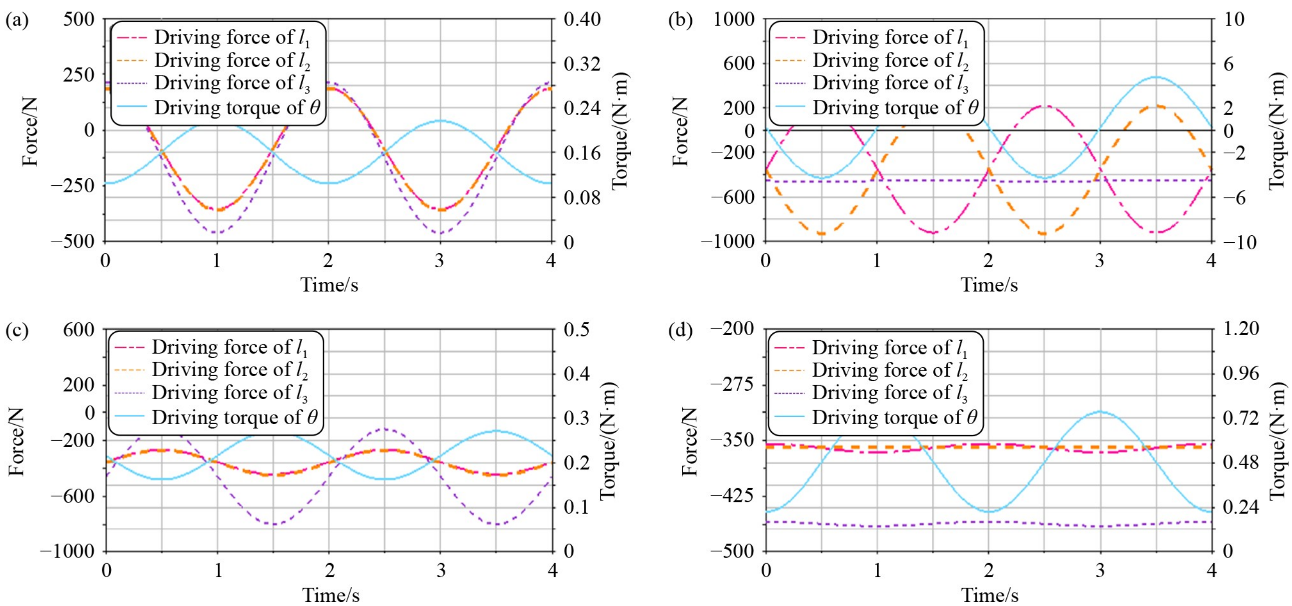

Fig. 22 Driving force and torque of actuators of the side-mounted leg in static simulation: (a) condition 1, (b) condition 2, (c) condition 3, and (d) condition 4.

characteristic, and analyzing the force of the actuator in this design is necessary. This section of content can be used to evaluate the mechanical performance of the leg mechanism and provide reference for further engineering design, such as part selection. Figures 21 and 22 show the static simulation of the side-mounted leg under different common force conditions and the results of driving force and torque of actuators. The main research objects are the driving forces on linear actuators l_1, l_2, and l_3 and the driving torque on the rotary actuator θ (Fig. 21(a)). First, the statics of the leg mechanism is analyzed in ADAMS. Assuming that the joints of the leg are locked, the driving force required to lock each joint is statically balanced with the external load on the leg. The initial configuration of the moving platform is defined as follows: $\alpha = \beta = \gamma = 0°$, $x = 0$ mm, $y = 200$ mm, and $z = 582$ mm. On the basis of different common force conditions of the leg, the driving forces or moments are solved:

(1) When the attitude of the rover shifts or the rover runs on an uneven road, its legs are subjected to gravity, and a support force changes along the y-axis direction (G and F_1 in Fig. 21(a)). In ADAMS, we define F_1 to follow its time-varying function $F_1(t) = 100\sin(\pi t - \pi/2) + 100$. The simulation result is shown in Fig. 22(a).

(2) When the rover remains stationary, the legs are subjected to gravity, a supporting force, and static friction along the x-axis (shown as G, N, and F_2 in Fig. 21(b)). Considering the weight of the rover, the supporting force is set as N = 200 N; we define F_2 to follow its time-varying function $F_2(t) = 200 \times 0.25\sin(\pi t)$ to simulate the static friction force for the leg-end on the road with different surface smoothness. The simulation result is shown as Fig. 22(b).

(3) When the rover remains stationary, the legs are subjected to gravity, a supporting force, and static friction along the z-axis (shown as G, N, and F_3 in Fig. 21(c)). The supporting force is set as N = 200 N; we define F_3 to follow its time-varying function $F_3(t) = 200 \times 0.25\sin(\pi t)$ to simulate the static friction force from the z-axis on different contact surfaces. The simulation result is shown in Fig. 22(c).

(4) The leg remains stationary. If the leg-end rotates around the y-axis, in addition to gravity and supporting force, then it will receive a torque caused by friction (shown as G, N, and M in Fig. 21(d)). The supporting force is set as N = 200 N; we define M to follow its time-varying function $M(t) = 2/3 \times 100(\sin(\pi t + \pi/2) - 1) \times 0.1$ to simulate a friction torque varying periodically from zero. The simulation result is shown in Fig. 22(d).

Based on the simulation results, most of the driving forces for static equilibrium are provided by linear actuators l_1, l_2, and l_3 because of the 3-U$\underline{\text{P}}$RU&$\underline{\text{R}}$RRR mechanism design in the legs. Given the self-locking property of the lead screw, if the linear actuator selects the lead screw, then it can greatly reduce the energy consumption of the leg while maintaining static balance. Under all simulation conditions, the driving force applied by each actuator is continuous and smooth without sudden change. In our design, the rated driving force of the linear actuator is 2 kN, and the rated torque of the rotary actuator is 40 N·m. The overall static performance of the leg mechanism is good.

In addition to static analysis, the mechanical properties of the leg in motion must also be analyzed. When the leg mechanism moves in accordance with the given trajectory, it is susceptible to the influence of inertia force. In ensuring the stability of the leg mechanism, the driving forces that maintain the dynamic balance must be measured. When the side-mounted leg moves without a load (for example, adjusting posture and stepping while being suspended), it is subjected to its own gravity and inertial forces. In ADAMS, two kinds of commonly used composite motion are selected for the kinetostatic simulation:

(1) The moving platform drives the leg-end to do a composite translation in the x–y plane, with the following trajectories:

$$\begin{cases} x(t) = 150\sin(\pi t/200), \\ y(t) = 60\sin(\pi t/400 + 3\pi/2) + 260. \end{cases} \tag{42}$$

This simulation result is shown in Fig. 23.

(2) The position of the moving platform does not move, only adjusting the posture of the leg-end with the following trajectory (the attitude angle covers the limit pose):

$$\begin{cases} \alpha'(t) = \pi/12 \times \sin(\pi t/200 - \arcsin(1/3)) + \pi/36, \\ \gamma'(t) = \pi/6 \times \sin(\pi t/400). \end{cases} \tag{43}$$

This simulation result is shown in Fig. 24.

Based on the abovementioned simulation results, in maintaining dynamic balance, each driving force curve is continuous and smooth. The driving forces applied by the linear actuators do not exceed 600 N, and the driving torque applied by the rotary actuator does not exceed 30 N·m. Furthermore, the leg has a good static dynamic performance.

6 Locomotion simulation of the quadruped earth rover BJTUBOT

In verifying the flexibility and function of the side-mounted (3-U$\underline{\text{P}}$RU&$\underline{\text{R}}$RRR)&$\underline{\text{R}}$ hybrid leg mechanism, we equipped it on the virtual model of our rover BJTUBOT. A 3D model of this quadruped robot is illustrated in Fig. 25. Based on this model, simulations of some LTs are performed. The CoppeliaSim simulation environment used in our research contains gravity, friction, inertia, and other dynamic factors that can demonstrate the running state of the rover.

6.1 Forms of motion of the leg mechanism in simulation

As shown in Fig. 25, we define the forward direction of the rover as the u positive direction. The upward direction perpendicular to the top of the rover body is the w positive direction, and that along the left side of the rover is the v positive direction. In facilitating the design of the basic locomotion form of the rover in the simulation, the DOFs of the leg must be summarized into five basic MFs.

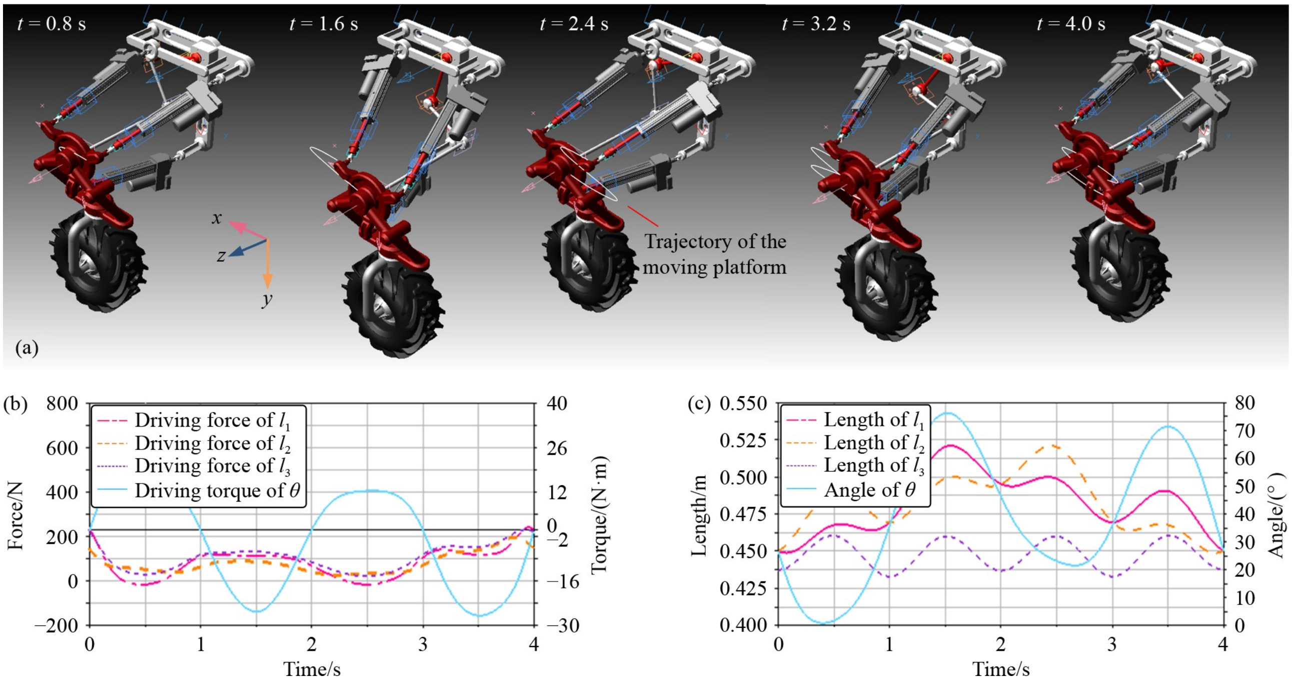

Fig. 23 Kinetostatic simulation for a composite translation of the leg: (a) timing diagram, (b) driving force and torque of actuator, and (c) position of actuator.

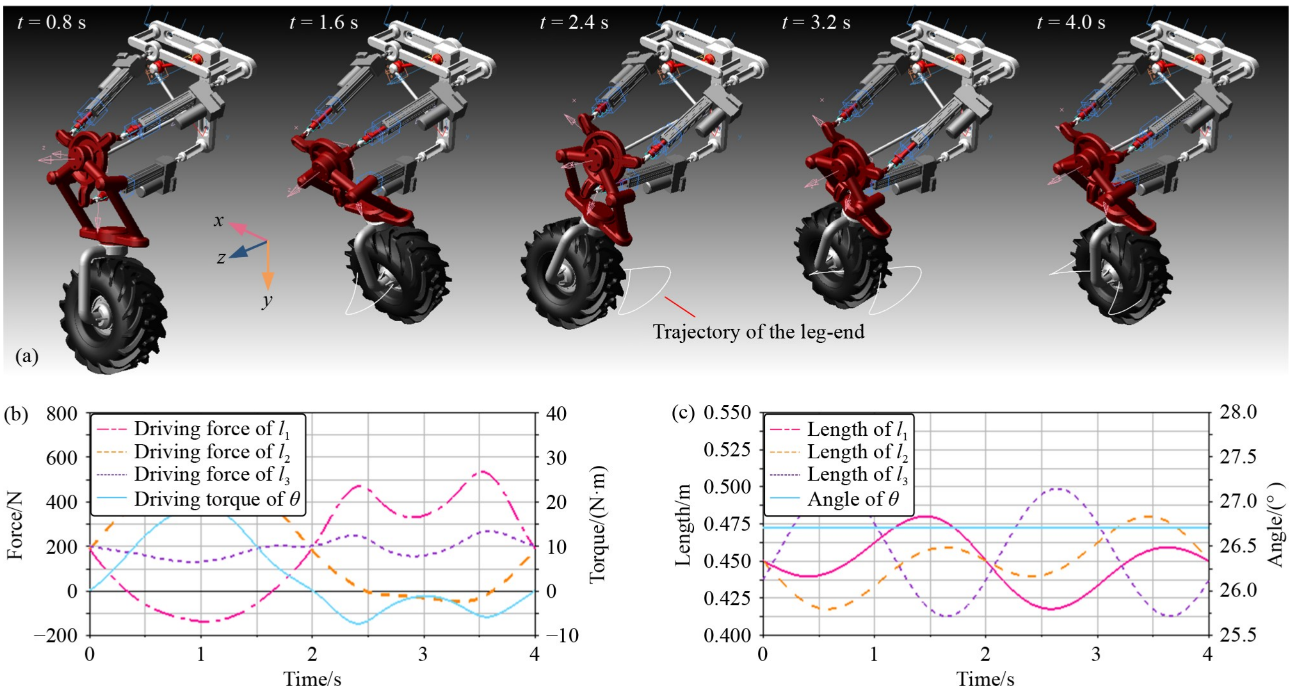

Fig. 24 Kinetostatic simulation for posture adjustment of the leg: (a) timing diagram, (b) driving force and torque of actuator, and (c) position of actuator.

Therefore, as described in Subsection 3.2, the basic MFs of each side-mounted (3-U$\underline{P}$RU&$\underline{R}$RRR)&$\underline{R}$ hybrid leg mechanism are as follows:

MF1. The moving platform rotates the angle γ' ($\gamma' = \gamma$) around $\$_1$. The wheel swings with the leg (Fig. 26(a)).

MF2. The moving platform translates along the y-axis, and the wheel rise and fall with the leg (Fig. 26(b)).

MF3. The leg mechanism translates along the x-axis. If the wheel is in the passive mode (the motor on the wheel is unpowered and does not apply torque), then it can roll

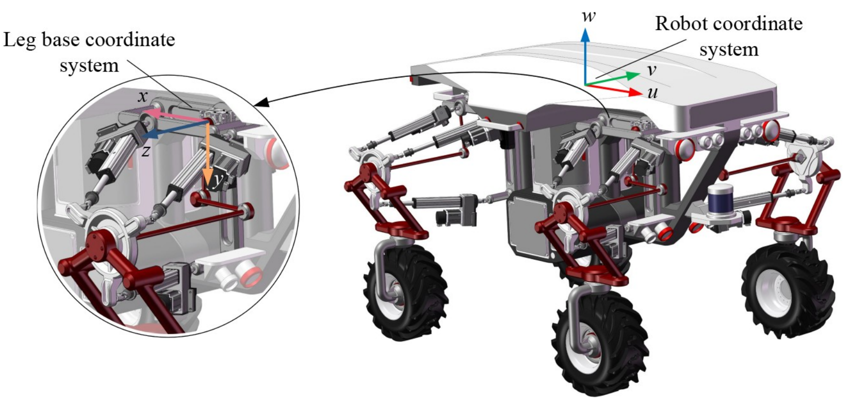

Fig. 25 Model of the quadruped rover BJTUBOT using the novel side-mounted 3-U$\underline{\text{P}}$RU&$\underline{\text{R}}$RRR&$\underline{\text{R}}$ hybrid leg mechanism.

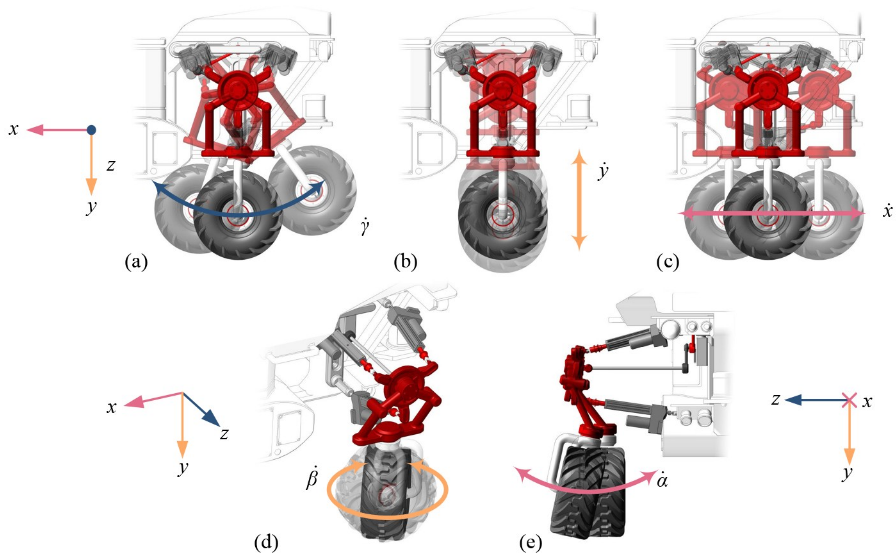

Fig. 26 Different forms of motion of the side-mounted leg mechanism in the virtual model of BJTUBOT for simulation: (a) MF1, (b) MF2, (c) MF3, (d) MF4, and (e) MF5.

passively on the ground when it follows the leg mechanism. If the wheel is in the active mode (the motor on the wheel is powered on and holds torque), then it can only slide on the ground (depending on the force of friction) when it follows the leg mechanism (Fig. 26(c)).

MF4. The wheel rotates the angle φ ($\varphi = \beta$) around $\$_2$, but its position does not change (Fig. 26(d)).

MF5. The moving platform rotates the angle α' ($\alpha' = \alpha$) around $\$_3$. The leg swings (Fig. 26(e)).

6.2 Locomotion tasks and simulation of the rover

As described in Subsection 3.2, if the four side-mounted legs of the rover respectively or simultaneously perform the abovementioned MFs based on certain rules, then the whole rover can achieve different LTs. Notably, the wheels of the rover contain drive motors. In active mode, the wheels can hold torque and drive the rover, whereas in the passive mode, they are used as passive wheels. Afterward, we will briefly introduce the basic LTs of the rover, give the trajectories of its leg-ends or its body's center of mass (CoM), and verify its performance through the corresponding simulations:

LT1. By combining MF1, MF4, and MF5, the wheelbase and support polygon of the rover can be adjusted, and the robot can achieve omnidirectional motion (there are only straight lines in the trajectory of leg-end shown in Fig. 27). As shown in Figs. 27(a)–27(c), the rover can increase or decrease the u-direction wheelbase by making the leg perform MF1. As shown in Figs. 27(e) and 27(f), all wheels can rotate 90° by executing MF4. Thus, the rover can move along the v-direction. As shown in Figs. 27(f) and 27(g), the rover can change the wheelbase in the v-direction by making the leg perform MF5.

LT2. By implementing MF4, the different rotation angles of the inner and outer wheels can lead to Ackermann steering of the rover (Fig. 28). By adjusting the rotation angle of the steering R joint in the (3-U$\underline{\text{P}}$RU&$\underline{\text{R}}$RRR)&$\underline{\text{R}}$ leg mechanism, the body of the rover can turn with different radius (Figs. 28(b)–28(d)).

LT3. By implementing MF4 or in combination with MF3, the rover can achieve a pivot steering locomotion (Fig. 29). By adjusting the rotation angle of the steering R joint, the rotation axes of the four wheels intersect with the *w*-direction axis, and then the rover can rotate in place. By altering the wheelbase of the rover (as shown in Figs. 29(d) and 29(f)), the rotation radius of pivot steering can be changed (Figs. 29(c), 29(e), and 29(h)).

LT4. By combining MF2 and MF4, the rover can achieve an active suspension function, thereby reducing the impact on rough terrain (Fig. 30). As shown in Figs. 30(a)–30(d), the road on one side of the rover is undulating. If the suspension is not available, then the rover will experience great turbulence on uneven terrain, and its body can hardly maintain balance. As shown in Figs. 30(a) and 30(e)–30(g), based on the information sent by acceleration sensors, the leg can use MF2 to make an active displacement along the *z*-direction to effectively adjust the attitude of the rover, and the CoM trajectory fluctuates regularly and gently. Furthermore, MF4 can adjust the forward direction of the rover to make it move smoothly and more balanced.

LT5. By combining MF2 and MF3, the rover achieves the basic walking locomotion (Fig. 31). MF2 and MF3 can make the leg move in the x–y plane without changing the attitude, thereby allowing the leg-end to follow the simplest gait trajectory. Figures 31(a)–31(d) show the first cycle of the locomotion to allow the rover moves from the initial posture to the gait. Figures 31(e)–31(l) show two cycles of walking locomotion. If MF1 and MF4 are executed simultaneously, then walking can be more sophisticated and adaptive.

In addition to the abovementioned basic tasks, we also

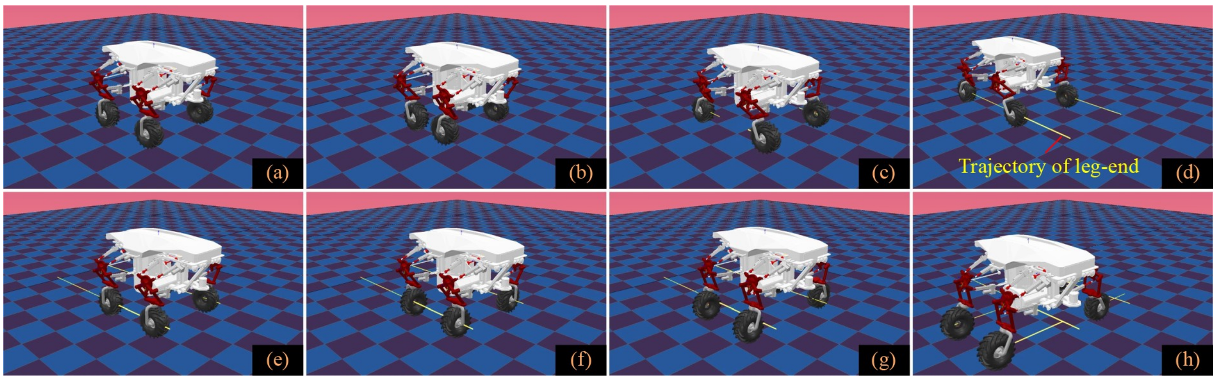

Fig. 27 Omnidirectional locomotion of the rover: (a) t = 0 s, (b) t = 1 s, (c) t = 3 s, (d) t = 5 s, (e) t = 10 s, (f) t = 11 s, (g) t = 13 s, and (h) t = 14 s.

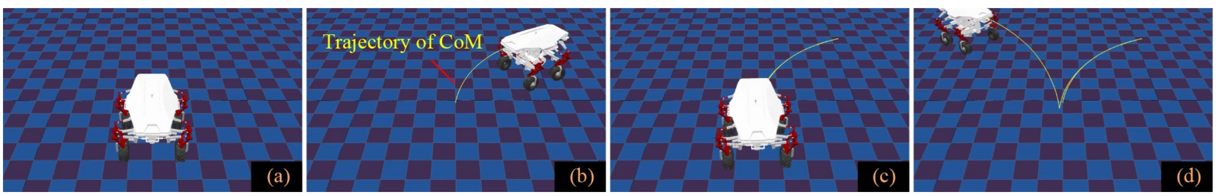

Fig. 28 Ackerman steering locomotion of the rover: (a) t = 0 s, (b) t = 5 s, (c) t = 12 s, and (d) t = 22 s. CoM: center of mass.

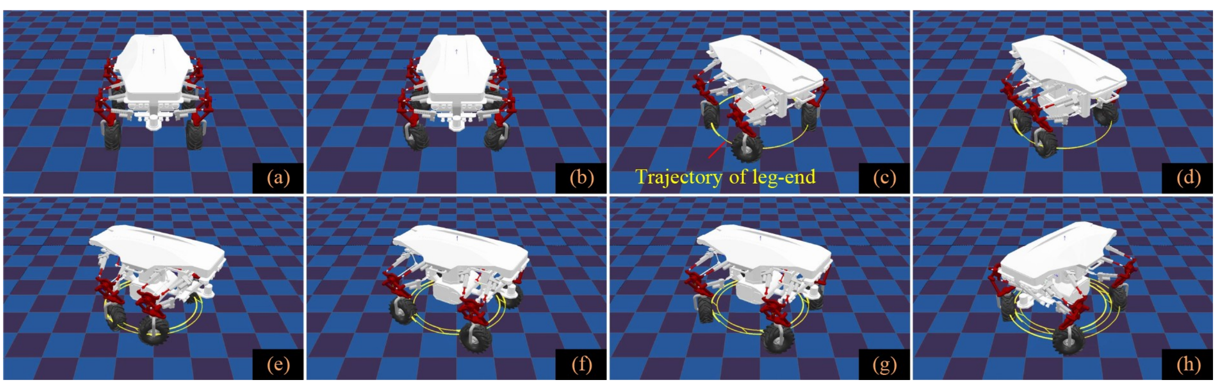

Fig. 29 Pivot steering locomotion of the rover: (a) t = 0 s, (b) t = 1 s, (c) t = 9 s, (d) t = 14 s, (e) t = 20s, (f) t = 25 s, (g) t = 26 s, and (h) t = 28 s.

simulated some more special tasks: When the rover attempts to pass through a low obstacle, it will execute MF2 first (Figs. 32(a) and 32(b)). However, as shown in the CoM trajectory, this form of motion is not effective because of the limited range of motion. After executing MF1 (Fig. 32(c)), the rover can reduce the body height, thereby achieving the crawling locomotion (Fig. 32(d)). Moreover, jumping can be an efficient form of the obstacle crossing task (Fig. 33). During jumping, the height and acceleration of taking off cannot be ensured by applying MF2 and MF3 alone because of the limits of motion range and actuators' performance. Thus, by combining MF1 and taking advantage of the rotational motion, the jumping height can be effectively improved. In addition, the CoM trajectory is smooth, which indicates that the rover can maintain the dynamic balance in the air by swiftly adjusting MF1.

By simulating the LTs of the rover, it can verify the

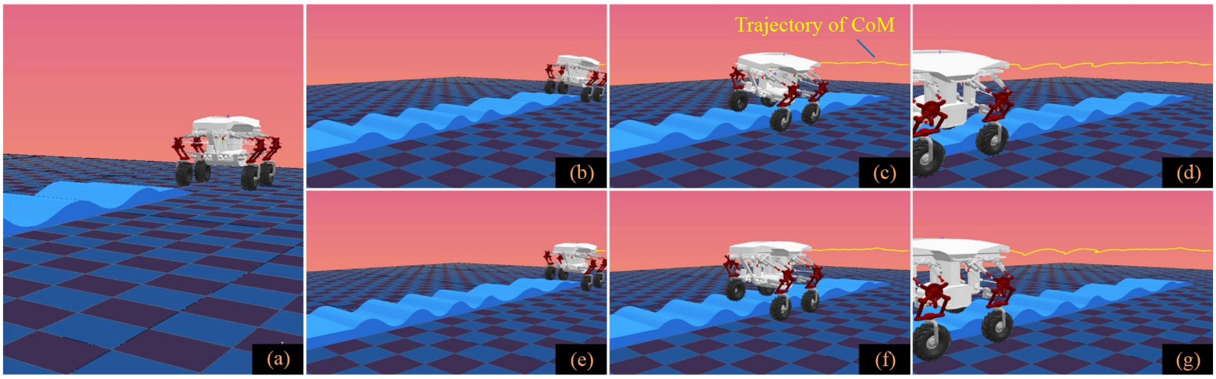

Fig. 30 Active suspension system function of the rover: (a) $t = 0$ s, (b) $t = 4$ s without suspension, (c) $t = 8$ s without suspension, (d) $t = 11$ s without suspension, (e) $t = 4$ s with suspension, (f) $t = 8$ s with suspension, and (g) $t = 11$ s with suspension. CoM: center of mass.

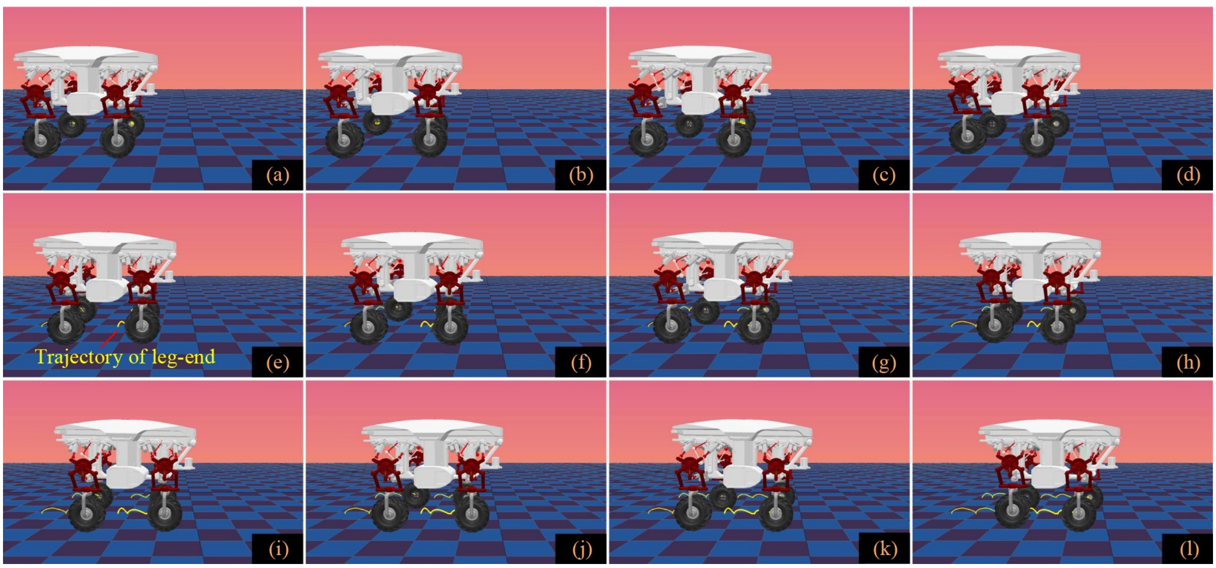

Fig. 31 Basic walking locomotion of the rover: (a) $t = 0$ s, (b) $t = 1$ s, (c) $t = 2$ s, (d) $t = 3$ s, (e) $t = 4$ s, (f) $t = 5$ s, (g) $t = 6$ s, (h) $t = 7$ s, (i) $t = 8$ s, (j) $t = 9$ s, (k) $t = 10$ s, and (l) $t = 11$ s.

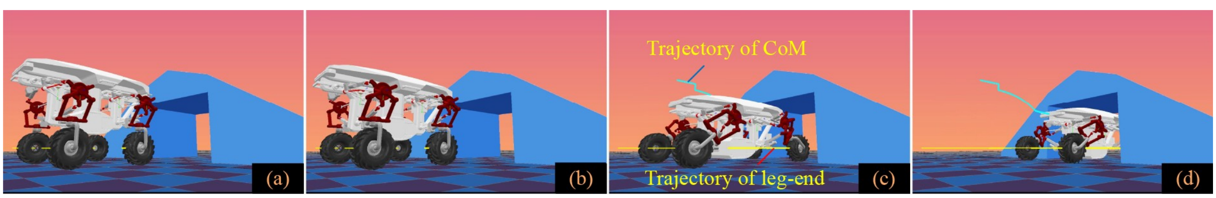

Fig. 32 Crawling locomotion of the rover: (a) $t = 0$ s, (b) $t = 4$ s, (c) $t = 7$ s, and (d) $t = 10$ s. CoM: center of mass.

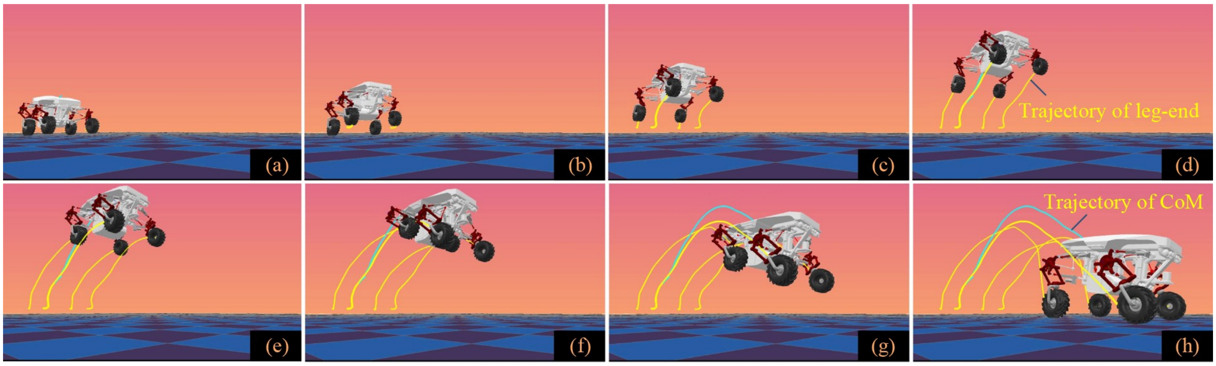

Fig. 33 Jumping locomotion of the rover: (a) $t = 0$ s, (b) $t = 1$ s, (c) $t = 2$ s, (d) $t = 4$ s, (e) $t = 8$ s, (f) $t = 10$ s, (g) $t = 12$ s, and (h) $t = 14$ s. CoM: center of mass.

validity of the side-mounted leg mechanism design. By integrating different forms of motion, the leg mechanism can enable the rover to multi-task with flexibility.

7 Conclusions

This paper presents a novel side-mounted 3R2T 5-DOF leg mechanism for an earth rover BJTUBOT. Based on screw theory, the desired MFs of the leg mechanism are introduced on the basis of the LTs of the rover. In achieving these MFs, two feasible side-mounted configurations of the leg are presented. Based on the constraint synthesis method, some asymmetric structures are listed for designing the novel leg. Utilizing the 6-DOF limbs with an L_{1F1C} limb, a more concise and efficient (3-U$\underline{\text{P}}$RU&$\underline{\text{R}}$RRR)&$\underline{\text{R}}$ hybrid leg mechanism is designed. The inverse kinematics and singularity configurations of this mechanism are analyzed. The workspace of the leg is given, which indicates that it can complete spatial tasks. The dexterity and global performance of the leg mechanism indicate its flexibility, whereas the static and kinetostatic simulations indicate that the leg has good mechanical properties. Furthermore, a virtual prototype of the earth-quadratic rover is built. Its basic and special LTs such as omnidirectional motion, active suspension, steering, walking, crawling, and jumping have been simulated. The simulation results demonstrate the high flexibility of the side-mounted leg, which allows the rover to multi-task. The design process mentioned in this paper can also provide reference for the construction of other wheeled-leg robots in specific fields.

Nomenclature

Abbreviations

C	Cylindrical joint
COM	Center of mass
DOF	Degree-of-freedom
GCI	Global conditioning index
L_{1F1C}	Passive constraining limb provides both a constraint force and a constraint couple
LCI	Local condition index
LT	Locomotion task
MF	Motion form
P	Prismatic joint
$\underline{\text{P}}$	Prismatic joint with actuation
R	Revolute
$\underline{\text{R}}$	Revolute joint with actuation
R_1	Type-1 revolute joint
R_2	Type-2 revolute joint
S	Spherical joint
T	Translation
U	Universal joint

Variables

$\boldsymbol{a}_i$	Vector $\overrightarrow{O_B A_i}$
${}^{B}\boldsymbol{a}_i$	$\boldsymbol{a}_i$ in the base coordinate
$\|\boldsymbol{A}\|$	Frobenius norm of matrix $\boldsymbol{A}_{m\times n}$
$\boldsymbol{b}_i$	Vector $\overrightarrow{O_P B_i}$
${}^{B}\boldsymbol{b}_i$	$\boldsymbol{b}_i$ in the base coordinate
d	Dimension of the wrench system
$\boldsymbol{d}$	Vector $\overrightarrow{CD}$
$\boldsymbol{d}'$	Vector $\overrightarrow{O_B D'}$
$\boldsymbol{e}$	Vector $\overrightarrow{DE}$
$\boldsymbol{e}'$	Vector $\overrightarrow{O_B E'}$
f	Constraint force
F	A support force or static friction
F_1	Support force along the y-axis
F_2, F_3	Static frictions along the x- and z-axis, respectively
$F_1(t)$, $F_2(t)$, $F_3(t)$	Time-varying functions of F_1, F_2, and F_3, respectively
G	Gravity force

h	Height of the side-mounted base along the y-axis
$\boldsymbol{J}$	Jacobian matrix of the 3-UPRU&RRRR parallel mechanism
$\boldsymbol{J}_{\mathrm{c\_RRRR}}$	Constraint Jacobian for the RRRR limbs
$\boldsymbol{J}_{\mathrm{k\_UPRU}}$	Actuation Jacobian for the UPRU limbs
$\boldsymbol{J}_v$	Linear velocity mapping part of $\boldsymbol{J}$
$\boldsymbol{J}_\omega$	Angular velocity mapping part of $\boldsymbol{J}$
$\boldsymbol{k}$	Vector $\overrightarrow{O_\mathrm{P}K}$
${}^\mathrm{B}\boldsymbol{k}$	$\boldsymbol{k}$ in the base coordinate
${}^\mathrm{P}\boldsymbol{k}$	$\boldsymbol{k}$ in the moving platform coordinate
${}^\mathrm{W}\boldsymbol{k}$	$\boldsymbol{k}$ in the wheel coordinate
$k(\boldsymbol{J})$	Condition number of the Jacobian matrix $\boldsymbol{J}$
l_i	Length of the vector $\overrightarrow{A_iB_i}$
$\boldsymbol{l}_i$	Vector $\overrightarrow{A_iB_i}$
$\dot{l}_i$	Linear velocity of the P joint
$l_{\max}$	Maximum length of the P joint
$l_{\min}$	Minimum length of the P joint
$\dot{\boldsymbol{L}}$	Vector which contains all velocities of the P joints
m	Constraint couple
M	Torque caused by friction
$M(t)$	Time-varying function of M
N	Support force
O_B	Original point of the base coordinate system
O_P	Original point of the moving platform coordinate system
O_W	Original point of the leg-end coordinate system
$\boldsymbol{p}$	Vector $\overrightarrow{O_\mathrm{B}O_\mathrm{P}}$
$\boldsymbol{p}_\mathrm{W}$	Vector $\overrightarrow{O_\mathrm{B}O_\mathrm{W}}$
${}^\mathrm{B}\boldsymbol{p}_\mathrm{W}$	Position vector of the leg-end in the base coordinate
$\dot{q}_{ij}$	Intensity of the jth joint in the ith limb
$\dot{\boldsymbol{Q}}$	Velocity vector of all joints
$\boldsymbol{r}$	Location vector of the twist $\boldsymbol{\$}$
$\boldsymbol{r}_i$	Location vector of the ith twist or screw $\boldsymbol{\$}_i$
$\boldsymbol{r}_d^\mathrm{r}$	Location vector of the dth constraint screw $\boldsymbol{\$}_d^\mathrm{r}$
${}^\mathrm{B}\boldsymbol{R}_\mathrm{P}$	Rotation matrix from the moving platform frame to the base frame
${}^\mathrm{B}\boldsymbol{R}_\mathrm{W}$	Rotation matrix from the leg-end frame to the base frame
${}^\mathrm{P}\boldsymbol{R}_\mathrm{W}$	Rotation matrix from the leg-end frame to the moving platform frame
${}^\mathrm{W}\boldsymbol{R}_\mathrm{P}$	Inverse of ${}^\mathrm{P}\boldsymbol{R}_\mathrm{W}$
$\boldsymbol{s}$	Direction vector of the twist $\boldsymbol{\$}$
$\boldsymbol{s}_i$	Direction vector of the ith twist or screw $\boldsymbol{\$}_i$
$\boldsymbol{s}_{ij}$	Direction vector of $\boldsymbol{\$}_{ij}$
$\boldsymbol{s}_d^\mathrm{r}$	Direction vector of the dth constraint screw $\boldsymbol{\$}_d^\mathrm{r}$
t	Time
$\boldsymbol{u}_{li}$	Unit vector of P joint
$\boldsymbol{u}_d$	Unit vector of the linkage CD
${}^\mathrm{B}\boldsymbol{u}_{li}$	$\boldsymbol{u}_{li}$ in the base coordinate
${}^\mathrm{B}\boldsymbol{v}$	Vector $\boldsymbol{v}$ in the base frame
${}^\mathrm{B}\boldsymbol{v}_{O_\mathrm{P}}$	Linear velocity of moving platform
${}^\mathrm{P}\boldsymbol{v}$	Vector $\boldsymbol{v}$ in the moving platform frame
${}^\mathrm{W}\boldsymbol{v}$	Vector $\boldsymbol{v}$ in the leg-end frame
w	Width of the side-mounted base along the x-axis
$\boldsymbol{w}$	Vector $\overrightarrow{KO_\mathrm{W}}$
WS	Workspcae
x	x-axis of the base coordinate system
$\dot{x}$	Velocity in the x direction
x_P	x-axis of the moving platform coordinate system
$x(t)$	Position function on the x-axis
$\dot{\boldsymbol{X}}$	Velocity of moving platform
y	y-axis of the base coordinate system
$\dot{y}$	Velocity in the y direction
y_P	y-axis of the moving platform coordinate system
$y(t)$	Position function on the y-axis
z	z-axis of the base coordinate system
z_P	z-axis of the moving platform coordinate system
α	Attitude angle about the x-axis
$\dot{\alpha}$	Velocity of α
α'	Rotation angle about the x_P-axis
$\alpha'(t)$	Orientation function about α'
β	Attitude angle about the y-axis
$\dot{\beta}$	Velocity of β
γ	Attitude angle about the z-axis
$\dot{\gamma}$	Velocity of γ
γ'	Rotation angle about the z_P-axis
$\gamma'(t)$	Orientation function about γ'
η_i	Value of GCI
η_v, η_ω	GCI of the linear and angular motions, respectively
θ	Rotation angle of the R joint in the RRRR limb
$\dot{\theta}$	Angular velocity of active R joint
$\dot{\theta}_{in}$	Intensity or angular velocity of the passive joints
φ	Rotation angle of the steering R joint connected with the leg-end
${}^\mathrm{B}\boldsymbol{\omega}$	Angular velocity of moving platform
$\delta\dot{\boldsymbol{Q}}$	Driving velocity deviation
$\boldsymbol{\$}$	A screw or a twist
$\boldsymbol{\$}^\mathrm{r}$	A wrench system
$\boldsymbol{\$}_i$	ith twist or screw
$\boldsymbol{\$}_{ij}$	Unit screw of the jth joint in the ith limb
$\boldsymbol{\$}_\mathrm{P}$	Instantaneous twist of the moving platform
$\boldsymbol{\$}_d^\mathrm{r}$	dth constraint screw
$\boldsymbol{\$}_i^\mathrm{r}$	Reciprocal screws for the ith UPRU limb
$\delta\boldsymbol{\$}_\mathrm{P}$	Velocity deviation of the moving platfrom

Acknowledgements This work was supported by the National Natural Science Foundation of China (Grant No. 52275004).

References

1. Schilling K, Jungius C. Mobile robots for planetary exploration. IFAC Proceedings Volumes, 1995, 28(11): 109–119
2. Lindemann R A, Voorhees C J. Mars exploration rover mobility assembly design, test and performance. In: Proceedings of 2005 IEEE International Conference on Systems, Man and Cybernetics. Waikoloa: IEEE, 2005, 450–455
3. Arvidson R E, Iagnemma K D, Maimone M, Fraeman A A, Zhou F, Heverly M C, Bellutta P, Rubin D, Stein N T, Grotzinger J P, Vasavada A R. Mars science laboratory curiosity rover megaripple crossings up to Sol 710 in gale crater. Journal of Field Robotics, 2017, 34(3): 495–518
4. Li C L, Liu J J, Ren X, Zuo W, Tan X, Wen W B, Li H, Mu L L, Su Y, Zhang H B, Yan J, Ouyang Z Y. The Chang'E 3 mission overview. Space Science Reviews, 2015, 190(1–4): 85–101
5. Tian H, Zhang T Y, Jia Y, Peng S, Yan C L. Zhurong: features and mission of China's first Mars rover. The Innovation, 2021, 2(3): 100121
6. Patel N, Slade R, Clemmet J. The ExoMars rover locomotion subsystem. Journal of Terramechanics, 2010, 47(4): 227–242
7. Hutter M, Gehring C, Jud D, Lauber A, Bellicoso C D, Tsounis V, Hwangbo J, Bodie K, Fankhauser P, Bloesch M, Diethelm R, Bachmann S, Melzer A, Hoepflinger M. ANYmal—a highly mobile and dynamic quadrupedal robot. In: Proceedings of 2016 IEEE/RSJ International Conference on Intelligent Robots and Systems (IROS). Daejeon: IEEE, 2016, 38–44
8. Buchanan R, Wellhausen L, Bjelonic M, Bandyopadhyay T, Kottege N, Hutter M. Perceptive whole-body planning for multilegged robots in confined spaces. Journal of Field Robotics, 2021, 38(1): 68–84
9. Lee J, Hwangbo J, Wellhausen L, Koltun V, Hutter M. Learning quadrupedal locomotion over challenging terrain. Science Robotics, 2020, 5(47): eabc5986
10. Bartsch S, Birnschein T, Römmermann M, Hilljegerdes J, Kühn D, Kirchner F. Development of the six-legged walking and climbing robot spaceclimber. Journal of Field Robotics, 2012, 29(3): 506–532
11. Bartsch S, Manz M, Kampmann P, Dettmann A, Hanff H, Langosz M, von Szadkowski K, Hilljegerdes J, Simnofske M, Kloss P, Meder M, Kirchner F. Development and control of the multi-legged robot MANTIS. In: Proceedings of ISR 2016 the 47th International Symposium on Robotics. Munich: IEEE, 2016, 1–8
12. Endo G, Hirose S. Study on Roller-Walker (multi-mode steering control and self-contained locomotion). In: Proceedings of 2000 ICRA. Millennium Conference. IEEE International Conference on Robotics and Automation. Symposia Proceedings (Cat. No.00CH37065). San Francisco: IEEE, 2000, 2808–2814
13. Geilinger M, Poranne R, Desai R, Thomaszewski B, Coros S. Skaterbots: optimization-based design and motion synthesis for robotic creatures with legs and wheels. ACM Transactions on Graphics, 2018, 37(4): 1–12
14. Geilinger M, Winberg S, Coros S. A computational framework for designing skilled legged-wheeled robots. IEEE Robotics and Automation Letters, 2020, 5(2): 3674–3681
15. Bjelonic M, Bellicoso C D, de Viragh Y, Sako D, Tresoldi F D, Jenelten F, Hutter M. Keep rollin′—whole-body motion control and planning for wheeled quadrupedal robots. IEEE Robotics and Automation Letters, 2019, 4(2): 2116–2123
16. Medeiros V S, Jelavic E, Bjelonic M, Siegwart R, Meggiolaro M A, Hutter M. Trajectory optimization for wheeled-legged quadrupedal robots driving in challenging terrain. IEEE Robotics and Automation Letters, 2020, 5(3): 4172–4179
17. Pan Y, Gao F. A new six-parallel-legged walking robot for drilling holes on the fuselage. Proceedings of the Institution of Mechanical Engineers, Part C: Journal of Mechanical Engineering Science, 2014, 228(4): 753–764
18. Chen X B, Gao F, Qi C K, Tian X H, Wei L. Kinematic analysis and motion planning of a quadruped robot with partially faulty actuators. Mechanism and Machine Theory, 2015, 94: 64–79
19. Giewont S, Sahin F. Delta-Quad: an omnidirectional quadruped implementation using parallel jointed leg architecture. In: Proceedings of 2017 the 12th System of Systems Engineering Conference (SoSE). Waikoloa: IEEE, 2017, 1–6
20. Peng H, Wang J Z, Wang S K, Shen W, Shi D W, Liu D C. Coordinated motion control for a wheel-leg robot with speed consensus strategy. IEEE/ASME Transactions on Mechatronics, 2020, 25(3): 1366–1376
21. Li J H, Wang J Z, Wang S K, Peng H, Wang B M, Qi W, Zhang L B, Su H. Parallel structure of six wheel-legged robot trajectory tracking control with heavy payload under uncertain physical interaction. Assembly Automation, 2020, 40(5): 675–687
22. Lin R F, Guo W Z, Li M. Novel design of legged mobile landers with decoupled landing and walking functions containing a rhombus joint. Journal of Mechanisms and Robotics, 2018, 10(6): 061017
23. Lin R F, Guo W Z. Creative design of legged mobile landers with multi-loop chains based on truss-mechanism transformation method. Journal of Mechanisms and Robotics, 2021, 13(1): 011013
24. Campos A, Budde C, Hesselbach J. A type synthesis method for hybrid robot structures. Mechanism and Machine Theory, 2008, 43(8): 984–995
25. Dong C L, Liu H T, Yue W, Huang T. Stiffness modeling and analysis of a novel 5-DOF hybrid robot. Mechanism and Machine Theory, 2018, 125: 80–93
26. Wen K F, Nguyen T S, Harton D, Laliberté T, Gosselin C. A backdrivable kinematically redundant (6+3)-degree-of-freedom hybrid parallel robot for intuitive sensorless physical human–robot interaction. IEEE Transactions on Robotics, 2021, 37(4): 1222–1238
27. Smith J A, Sharf I, Trentini M. PAW: a hybrid wheeled-leg robot. In: Proceedings of 2006 IEEE International Conference on Robotics and Automation. Orlando: IEEE, 2006, 4043–4048
28. He J, Gao F. Type synthesis for bionic quadruped walking robots. Journal of Bionics Engineering, 2015, 12(4): 527–538
29. Zhang J Z, Jin Z L, Feng H B. Type synthesis of a 3-mixed-DOF protectable leg mechanism of a firefighting multi-legged robot based on GF set theory. Mechanism and Machine Theory, 2018, 130: 567–584

30. Cordes F, Dettmann A, Kirchner F. Locomotion modes for a hybrid wheeled-leg planetary rover. In: Proceedings of 2011 IEEE International Conference on Robotics and Biomimetics. Karon Beach: IEEE, 2011, 2586–2592
31. Cordes F, Kirchner F, Babu A. Design and field testing of a rover with an actively articulated suspension system in a Mars analog terrain. Journal of Field Robotics, 2018, 35(7): 1149–1181
32. Fang Y F, Tsai L W. Enumeration of a class of overconstrained mechanisms using the theory of reciprocal screws. Mechanism and Machine Theory, 2004, 39(11): 1175–1187
33. Gan D M, Liao Q Z, Dai J S, Wei S M. Design and kinematics analysis of a new 3CCC parallel mechanism. Robotica, 2010, 28(7): 1065–1072
34. Kong X W, Gosselin C M. Type synthesis of 3T1R 4-DOF parallel manipulators based on screw theory. IEEE Transactions on Robotics and Automation, 2004, 20(2): 181–190
35. Kong X W, Gosselin C M. Type synthesis of 5-DOF parallel manipulators based on screw theory. Journal of Robotic Systems, 2005, 22(10): 535–547
36. Habibi H, Shirazi K H, Shishesaz M. Roll steer minimization of McPherson-strut suspension system using genetic algorithm method. Mechanism and Machine Theory, 2008, 43(1): 57–67
37. Cherian V, Jalili N, Ayglon V. Modelling, simulation, and experimental verification of the kinematics and dynamics of a double wishbone suspension configuration. Proceedings of the Institution of Mechanical Engineers, Part D: Journal of Automobile Engineering, 2009, 223(10): 1239–1262
38. Kang H Y, Suh C H. Synthesis and analysis of spherical-cylindrical (SC) link in the McPherson strut suspension mechanism. Journal of Mechanical Design, 1994, 116(2): 599–606
39. Fang Y F, Tsai L W. Structure synthesis of a class of 4-DoF and 5-DoF parallel manipulators with identical limb structures. The International Journal of Robotics Research, 2002, 21(9): 799–810
40. Li Q C, Huang Z. Type synthesis of 4-DOF parallel manipulators. In: Proceedings of 2003 IEEE International Conference on Robotics and Automation (Cat. No.03CH37422). Taipei: IEEE, 2003, 755–760
41. Zhang D, Gosselin C M. Kinetostatic modeling of N-DOF parallel mechanisms with a passive constraining leg and prismatic actuators. Journal of Mechanical Design, 2001, 123(3): 375–381
42. Zhang D, Gosselin C M. Kinetostatic modeling of parallel mechanisms with a passive constraining leg and revolute actuators. Mechanism and Machine Theory, 2002, 37(6): 599–617
43. Joshi S A, Tsai L W. Jacobian analysis of limited-DOF parallel manipulators. Journal of Mechanical Design, 2002, 124(2): 254–258
44. Gosselin C, Angeles J. Singularity analysis of closed-loop kinematic chains. IEEE Transactions on Robotics and Automation, 1990, 6(3): 281–290
45. Angeles J, López-Cajún C S. Kinematic isotropy and the conditioning index of serial robotic manipulators. The International Journal of Robotics Research, 1992, 11(6): 560–571
46. Gosselin C, Angeles J. A global performance index for the kinematic optimization of robotic manipulators. Journal of Mechanical Design, 1991, 113(3): 220–226